A Method for Imaging Energetic Particle Precipitation with Subionospheric VLF Signals

Forrest Gasdia[1*] **and Robert A. Marshall**[1]

[1]Ann and H.J. Smead Aerospace Engineering Sciences, University of Colorado, Boulder, CO, USA.

Key Points:

- VLF propagation is more strongly influenced by the flux of precipitating particles than the energy distribution
- A Kalman filter is applied to observations simulated at an array of VLF receivers to estimate the underlying disturbed ionospheres
- The estimation method identifies the size and location of precipitation patches during daytime but is less effective at nighttime

*Current address, Arlington, VA, USA.

Corresponding author: Forrest Gasdia, `forrest.gasdia@colorado.edu`

Abstract

Energetic particle precipitation (EPP) is a key loss mechanism for radiation belt particles. Quantification of the precipitation loss rate feeds into the electron lifetimes used by radiation belt models and is needed to improve understanding of radiation belt dynamics. EPP deposits most of its energy in the D-region ionosphere, a layer so weakly ionized that it is not observed using standard ionosphere measurement techniques. However, very low frequency (VLF) radio signals propagate great distances because of the naturally occurring waveguide formed by Earth's surface and the D-region. If the ground conductivity is known along the propagation path to a receiver, then the amplitude and phase of a VLF transmitter signal can be used to infer the average conductivity of the D-region ionosphere. This article simulates the propagation of narrowband VLF signals through realistic ionosphere profiles enhanced by EPP. By using a distributed array of VLF receivers, the observations can be simultaneously inverted to estimate the spatial extent of a precipitation patch. These images of the ionosphere are generated using the local ensemble transform Kalman filter (LETKF). We demonstrate this method with several simulated observation experiments, including four EPP events. Precipitation patches are identified in daytime, but accurate estimation of nighttime ionospheres remains a challenge.

1 Introduction

One of the many phenomena that disturbs the D-region ionosphere is energetic particle precipitation (EPP). Radiation belt particles traversing Earth's magnetic field encounter an increasingly dense neutral atmosphere as they near Earth. Through interaction with neutral molecules, these precipitating particles are effectively lost from the radiation belts. Energy deposited through inelastic collisions and bremsstrahlung of higher energy electrons affects the chemistry of the lower ionosphere and neutral atmosphere (Krause, 1998; Randall et al., 2005, 2007).

EPP is just one of several competing processes that enhance or deplete electron populations of the radiation belts during and after solar storms (Reeves et al., 2003; Blum & Breneman, 2020). Quantifying the characteristics, relative significance, and relationships between the various source and loss mechanisms will improve forecasting of space weather (Millan & Thorne, 2007; Tu et al., 2010). In particular, uncertainty in the theoretical loss rate due to precipitation is responsible for differences between modeled and observed electron lifetimes (Marshall & Cully, 2020).

Several techniques have been used to observe precipitating energetic electrons. Particle detectors can directly monitor EPP from low Earth orbit, but most missions have not observed the entirety of the loss cone because of limited pitch angle resolution (Rodger et al., 2013). The ELFIN mission, consisting of a pair of CubeSats launched in 2018, is the first mission to accurately measure the energy and pitch angle of relativistic precipitating particles (Angelopoulos et al., 2020). Analysis and publication of ELFIN observations is ongoing, but other CubeSat missions have produced a range of estimates of the spatial scale of precipitation patches. Crew et al. (2016) found microbursts at least as small as 11 km, as limited by the nearest separation distance of the FIREBIRD satellites, and maximum sizes of about 120 km when mapped to the equator. Shumko et al. (2018) also analyzed FIREBIRD observations and found a spatially large microburst with radial and azimuthal scale sizes of at least (500 ± 10) km and (530 ± 10) km at the magnetic equator. The pair of AeroCube-6 CubeSats observed precipitating structures at several spatial scales (Blake & O'Brien, 2016). These observations seem to indicate there is both fine structure and broader areas of precipitation.

Below the ionosphere, balloon payloads observe X-rays emitted by bremsstrahlung which can be mapped back to the precipitating electron spectra. Dozens of flights of the Balloon Array for Radiation belt Relativistic Electron Losses (BARREL) missions have been flown (Millan et al., 2013; Woodger et al., 2015). Anderson et al. (2017) analyzes data from BARREL, FIREBIRD, and AeroCube-6 during the same EPP event and finds the precipitation region extends at least 4 h in local time, from $L = 5$ out to $L = 10$, and was present for nearly 9 hours. Electron density in the D-region is sufficiently enhanced by EPP to influence the propagation of subionospheric very low frequency (VLF) radio waves. Unlike other methods, stationary VLF receivers can monitor large spatial regions continuously. The Array for Broadband Observations of VLF/ELF Emissions (ABOVE) incorporates VLF receivers across Canada that monitor electromagnetic waves including the narrowband minimum-shift keying (MSK) signals of U.S Navy VLF transmitters (Cully et al., 2014). Forty energetic electron injection events observed by the Van Allen Probes mission were correlated with ABOVE receiver measurements to characterize the typical response of VLF propagation (Mauk et al., 2013; Ghaffari et al., 2020). The different propagation paths of the array were used to estimate bounds on the size of the detectable precipitation region as between 200 and 1000 km along one path and above $L = 6$. Similarly, the Antarctic-Arctic Radiation-belt (Dynamic) Deposition-VLF Atmospheric Research Konsortia (AARDDVARK) network consists of VLF receivers specifically for monitoring VLF transmitter signals across the polar regions (Clilverd et al., 2009). Clilverd et al. (2017) combines simultaneous BARREL and AARDDVARK observations of two events and finds precipitation regions having longitudinal dimensions of approximately 20° and 50°–70°. They were also able to reproduce the observed AARDDVARK amplitude perturbations using mono-energetic electron precipitation fluxes based on the BARREL observations.

Monitoring of VLF narrowband radio transmissions has long provided indirect insight into the D-region ionosphere and its response to perturbing phenomena (Wait, 1958; Clilverd et al., 1999; Silber & Price, 2017). The propagation of VLF waves is influenced by the conductivity of the ground and lower ionosphere, which together form the "Earth-ionosphere waveguide". Because changes in ionosphere conductivity change the field pattern in the waveguide, monitoring the electromagnetic field at a radio receiver is a form of remotely sensing the D-region. In D-region estimation, we assume the ground conductivity is perfectly known from published global conductivity maps, e.g. Morgan (1968); ITU-R (2015). If the ionosphere were also known, a propagation model could be used to compute the electric field that would be measured by a radio receiver in the waveguide. In estimation theory, this is called the forward modeling problem. The inverse problem reconstructs the ionosphere required to reproduce the field measured by real radio receivers, and the typical method of solution iteratively runs the forward model with different proposed ionospheres until the modeled and real observations match to within some tolerance.

Work has recently been undertaken to generate spatially-varying estimates or "images" of the D-region ionosphere over a large geographic region using arrays of VLF receivers (McCormick & Cohen, 2018; Gasdia & Marshall, 2019). Rather than inverting receiver observations to produce a path-average estimate of the D-region along individual propagation paths, these new estimation techniques leverage the underlying spatial correlation of the ionosphere to spread measurement information between paths. This is a difficult, ill-conditioned, nonlinear inverse problem, but the solution space can be reduced by weighting the problem towards physically likely ionospheres based on expectations from prior knowledge of the ionosphere.

These techniques appear promising for estimation of the D-region under typical conditions, but this article examines the imaging problem for realistic ionospheres that are strongly disturbed by EPP. We link together a series of models to generate a realistic ionosphere for simulating observations of narrowband VLF signals. Next, EPP-disturbed ionospheres are compared to the Wait exponential ionosphere from the perspective of subionospheric VLF propagation along the ground (Wait & Spies, 1964). Finally, we describe a D-region imaging methodology that builds upon Gasdia (2021) and apply it to VLF observations simulated under a variety of realistic EPP and undisturbed ionospheres.

2 Modeling EPP-Disturbed Ionospheres

The propagation of VLF waves through the Earth-ionosphere waveguide depends on a number of factors, including: ground conductivity, number density and collision frequency profiles of each constituent of the ionosphere, the curvature of Earth, the magnitude and direction of Earth's magnetic field, and the transmitter frequency. Several of these parameters vary along the propagation paths of VLF receiver networks, which are often greater than 1000 km in length. The Long-Wavelength Propagation Capability (LWPC) is a commonly used forward model that can generate receiver observations for user-specified ionospheres (McRae & Thomson, 2000; Chakraborty et al., 2016; Phanikumar et al., 2018). Other propagation models, such as finite-difference time-domain (FDTD) and finite-difference frequency-domain (FDFD) methods, require orders of magnitude more computation time (Marshall et al., 2017; Xu et al., 2019). For nonlinear inverse problems like D-region estimation, the forward model must be run many times, making a mode theory propagation model, like LWPC, the obvious choice. This work uses LWPC in the inversion process and the Longwave Mode Propagator (LMP) to simulate "real" observations of VLF signals through perturbed ionospheres (Gasdia & Marshall, 2021). LMP is also a mode theory propagation model, but it is more robust than LWPC and easily accommodates complicated multi-species ionosphere profiles. This section describes the models and process used to simulate realistic VLF observations through typical and EPP-disturbed ionospheres.

2.1 Ionosphere Profiles

The Glukhov, Pasko, and Inan (GPI) model is a basic chemical model for the lower ionosphere that consists of four kinds of charged particles: electrons, negative ions (e.g. ${O_2}^-$, ${CO_3}^-$, ${NO_2}^-$), light positive ions (e.g. ${O_2}^+$, NO^+), and heavy positive ion clusters (e.g. $H^+(H_2O)_n$), where the number densities of each are referred to as N_e, N^-, N^+, and N_x^+ (Glukhov et al., 1992). Lehtinen and Inan (2007) separated the negative ion category into light negative ions (e.g. ${O_2}^-$) and heavy negative ions (e.g. ${NO_3}^-$), denoted by N^- and N_x^-, to improve accuracy at heights below 50 km. The model simultaneously solves a set of four time-differential equations for the number density of each species at each altitude. The density of the fifth species is calculated from the charge neutrality condition. An ionization source Q is calculated as the source necessary to produce a steady state solution of the equations from initial background density profiles of e^-, O, O_2, and N_2, which are provided by other models. After establishing the equilibrium density profiles for each constituent, GPI can be run once more with an additional imposed ionization source, such as EPP. For this work, a custom implementation of GPI was written in the Julia programming language for improved performance using the default parameters from GPI version 5.4 of Lehtinen and Inan (2007).

NRLMSISE-00, accessed through the software package SatelliteToolbox.jl, provides the neutral number density, mass density, and temperature profiles for the GPI model and EPP ionization lookup table (discussed below) (Picone et al., 2002; Chagas et al., 2019). We use the Faraday International Reference Ionosphere (FIRI-2018) for the initial electron density profile. FIRI is a semi-empirical model of the undisturbed ionosphere based on an ion-chemical model adjusted for consistency with sounding rocket profiles (Torkar & Friedrich, 1983; Friedrich & Torkar, 2001; Friedrich et al., 2018). It effectively extends the International Reference Ionosphere (IRI) for the D-region down to about 60 km altitude or $10^6\,e^-/m^3$ (Bilitza et al., 2017). FIRI-2018 consists of 1980 profiles across 11 solar zenith angles between 0° and 130°, latitudes 0°, 15°, 30°, 45°, and 60° N, and three solar activity levels for the middle of each month of the year. We have developed a tool

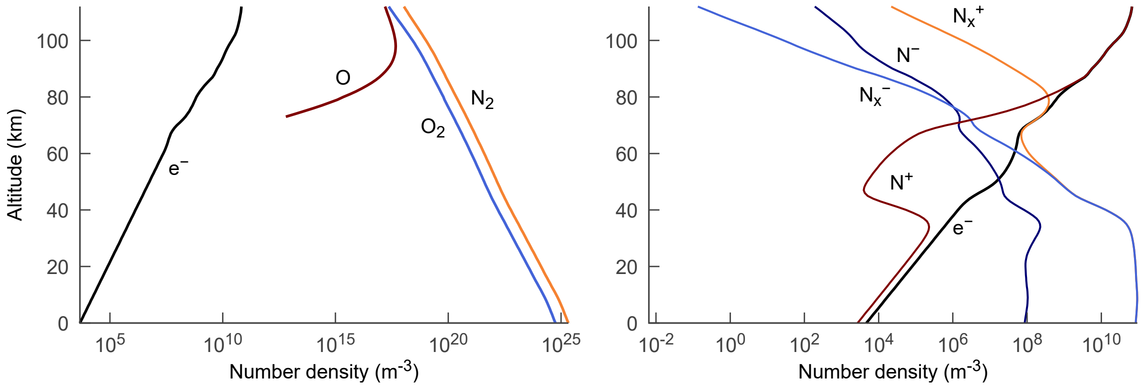

Figure 1. Left: NRLMSISE-00 neutral species and interpolated FIRI-2018 density profiles for 2020-03-01 2000Z at 60° N, 102° W (local daytime) (Picone et al., 2002; Friedrich et al., 2018). Right: Charge density profiles output from the GPI model using the profiles on the left as input (Lehtinen & Inan, 2007). Note the difference in scale along the horizontal axis.

that performs multidimensional linear interpolation across the solar zenith angle and latitude parameters to generate profiles that vary continuously over geographic latitude and longitude (Gasdia, 2022b).

Figure 1 shows profiles of the undisturbed daytime neutral atmosphere and ionosphere constituents before and after application of the GPI model. The FIRI profile uses a log-linear extrapolation from 60 km altitude down to the ground. These profiles are an example of those used by the Longwave Mode Propagator to simulate observations of narrowband VLF signals with a realistic undisturbed ionosphere.

2.2 Precipitation Modeling

Precipitating electrons deposit most of their energy between 40 and 100 km altitude, causing marked enhancements in the electron density of the D-region (Rees, 1963; Marshall & Bortnik, 2018). Recent studies have demonstrated that both the pitch angle and energy of radiation belt electrons have an important role in determining the ionization production of precipitation into the atmosphere (Randall et al., 2015; Tyssøy et al., 2016). Xu et al. (2020) applies the first-principles Energetic Precipitation Monte Carlo (EPMC) model to calculate ionization rate profiles produced by monoenergetic electrons with discrete pitch angles. EPMC was originally developed by Lehtinen et al. (1999) and extended over several years to simulate energetic electron precipitation effects (Marshall et al., 2014; Xu et al., 2018). The lookup table published by Xu et al. (2020) and implemented in Gasdia (2022a) produces an EPP-ionization rate profile with interpolation across altitude, precipitating electron energy and pitch angle distribution, and arbitrary neutral mass density profiles. The ionization rate profile (pairs/e^-/cm) can be multiplied by the precipitating electron flux ($e^-/cm^2/s$) for the ionization (pairs/cm^3/s) as a function of altitude.

Whittaker et al. (2013) used data from the electron flux instrument on the DEMETER spacecraft, sensitive from 90 keV to 2.2 MeV, to show that most distributions of precipitating electrons fit well to exponential or power-law energy distributions. In this work we assume the precipitating electrons have a uniform pitch angle distribution over 0° to 90° and an energy distribution modeled by the exponential function

$$f(E) = C_e \exp(-E/E_0). \tag{1}$$

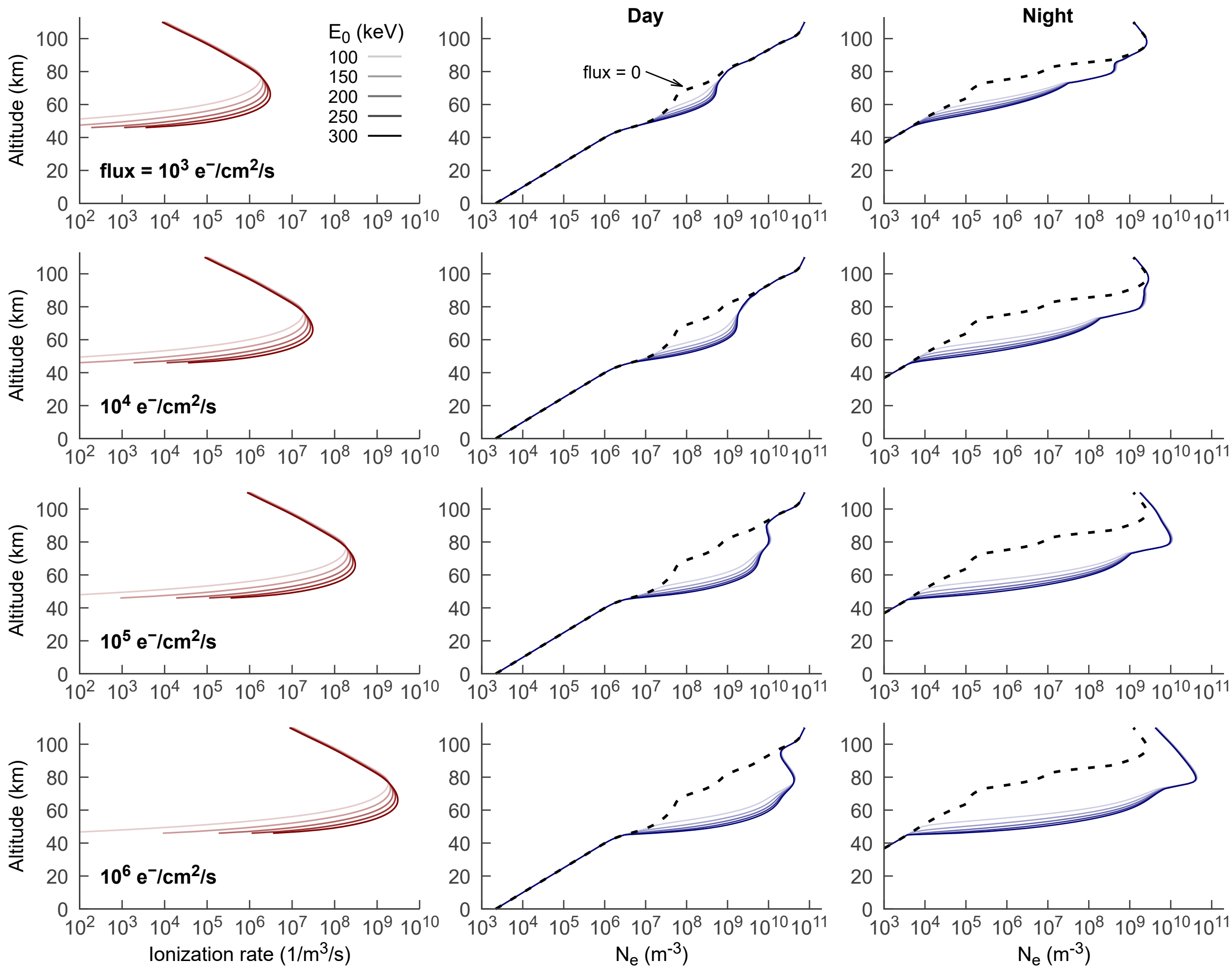

Figure 2. Ionization rate (left column) and electron density profiles for several exponential energy distributions and fluxes at day (middle column) and night (right column). The shade of each line corresponds to E_0 of the exponential energy distribution of the precipitating electrons (Whittaker et al., 2013). The black dashed line represents the undisturbed ionosphere.

Depending on the L-shell and Kp index, Whittaker et al. (2013) found the shape parameter E_0 varied between 100 and 300 keV. Examples of ionization and the electron density profiles output from GPI for typical day and night ionospheres are shown in Fig. 2 for several precipitating fluxes and values of E_0.

2.3 Defining the Earth-Ionosphere Waveguide

Each of the models discussed above are linked together to generate ionosphere profiles and simulated observations of transmitted narrowband VLF signals in the Earth-ionosphere waveguide. A flow chart of the process is shown in Fig. 3. In addition to the models previously discussed, the magnetic field vector at 60 km altitude is obtained from IGRF-13 for the appropriate time and location along the propagation path (Thébault et al., 2015). The ground conductivity map is the same one used by LWPC (Ferguson, 1998).

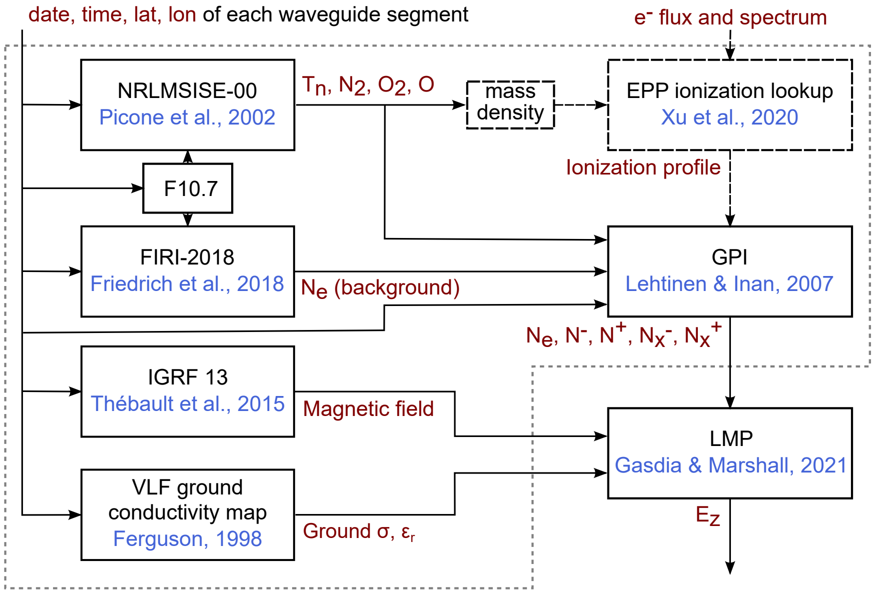

Figure 3. Diagram of the the process used to generate simulated VLF observations of realistic ionospheres, including when disturbed by energetic particle precipitation. The boxes contained in the gray dotted box provide output every 50 km along each propagation path to construct a segmented waveguide for the LMP propagation model. The two boxes drawn with black dashed lines are only active when EPP is present.

The mode theory propagation models LWPC and LMP define the Earth-ionosphere waveguide along a propagation path using a series of homogeneous segments and apply full-wave mode conversion at the boundaries between segments (Pappert & Smith, 1972). In this work each propagation path is split into 50 km segments. Therefore, all of the models contained inside the gray dashed bounding box in Fig. 3 are run every 50 km along the great circle path from transmitter to receiver. The complete segmented waveguide is then passed to LMP to generate the E_z field along the propagation path to the receiver.

3 Propagation Through EPP-Disturbed Ionospheres

This section presents simulations of subionospheric narrowband VLF propagation when the ionosphere is disturbed by energetic particle precipitation. First we examine propagation under an ionosphere defined by a constant conductivity profile along the entire path. Then we provide an example of simulated VLF receiver observations for spatially localized precipitation. This section provides context for understanding the requirements and limitations of inversion methods that can be used to image precipitation patches with real VLF data.

3.1 Effective Exponential Profiles

The VLF community commonly represents the D-region electron density using a profile derived from Wait and Spies exponential conductivity profile (Wait & Spies, 1964). The electron density N_e (e^-/m^3) as a function of height z (km) can be expressed as

$$N_e(z) = 1.43 \times 10^{13} \exp(-0.15h') \exp((\beta - 0.15)(z - h')) \tag{2}$$

where h' is a reference height (km) and β is a slope term (km^{-1}). Although this profile fails to capture the complex shape of the true D-region (e.g. Fig. 1), its use in propagation models matches real VLF data to within a few decibels under typical day and night conditions (Ferguson, 1980, 1992). Four-parameter models have recently been proposed to better fit observations of lightning-emitted VLF signals and narrowband signals along a rocket trajectory (McCormick & Cohen, 2021; Xu et al., 2021), but representing the altitude variation of ionosphere conductivity with only two parameters (h' and β) is useful for ionosphere estimation because it reduces the parameter space. Therefore, we estimate the ionosphere as defined using the two Wait ionosphere parameters, h' and β. In practice there are a relatively small number of VLF observations available when trying to estimate an ionosphere that varies spatially over a large geographic area. The inversion problem becomes increasingly ill-posed as the specification of the electron density with height is given additional degrees of freedom. This can be countered by regularization of the solution, but more experience applying this technique to real data is desired before investigating estimation with more complex representations of the ionosphere.

This section identifies the h' and β parameters that provide the best fit to VLF signals propagating under a completely EPP-disturbed ionosphere. In other words, we are seeking the exponential ionosphere that would be retrieved from VLF observations for an ionosphere disturbed by EPP. The E_z field of a 24 kHz transmitter is computed along the ground every 5 km out to 3000 km with a constant ocean-like ground ($\sigma = 4\,\mathrm{S\,m^{-1}}$, $\epsilon_r = 81$) and a vertical 50 µT magnetic field. The propagation model is run using a homogeneous (single segment) ionosphere defined by combinations of Wait parameters from an h' of 50 to 90 km every 0.5 km and a β of 0.2 to 1 km^{-1} every 0.05 km^{-1}. These values bracket the typical parameters of $h' = 70$ to 78 km and $\beta = 0.25$ to 0.4 km^{-1} at day and $h' = 83$ to 89 km and $\beta = 0.4$ to 0.7 km^{-1} at night with consideration for the lower altitude and steeper electron density profiles resulting from EPP (McRae & Thomson, 2000; Thomson et al., 2007; Thomson & McRae, 2009). The propagation model is run with a realistic EPP-disturbed ionosphere and compared to the Wait ionospheres using the mean absolute difference (MAD) of the signal amplitude and phase along the propagation path. For example, the amplitude MAD is computed as

$$A_{\mathrm{MAD}} = \frac{1}{n}\sum_{i=1}^{n} |A_{\mathrm{Wait},i} - A_{\mathrm{EPP},i}| \tag{3}$$

over a total of n signal amplitudes simulated every 5 km along the propagation path.

Figure 4 shows heatmaps of the amplitude and phase MAD for realistic unperturbed and EPP-perturbed daytime and nighttime ionospheres at 2020-03-01 2000Z and 2020-03-02 0500Z, respectively. The precipitating electron flux is $10^5\,\mathrm{e^-/cm^2/s}$ along the entire propagation path and the precipitating electrons have an exponential energy distribution with $E_0 = 200$ keV.

The lowest MAD (best fit) in Fig. 4 is located at approximately the same h' and β for both the amplitude and phase fits. Comparing the unperturbed and EPP-perturbed ionospheres, the EPP-perturbed ionosphere has shifted to a lower h'. This is expected because the EPP increases ionization at lower altitudes than the undisturbed ionosphere (Fig. 2). Although the amplitude maps exhibit multiple local minima, this can be resolved by incorporating phase information. At least for this particular configuration of transmitter and Earth-ionosphere waveguide, there is a unique representation of the EPP ionosphere by an exponential ionosphere within the range of reasonable h' and β. The local minima can also be excluded as a solution in estimation problems by exploiting the *a priori* expectation that the typical daytime D-region ionosphere has an h' around 75 km and the nighttime ionosphere has an h' around 85 km. This is discussed further in Section 4.

It is evident from Fig. 4 that long-path narrowband VLF observations have decreasing sensitivity to β as β increases. There is almost no sensitivity to β above approximately

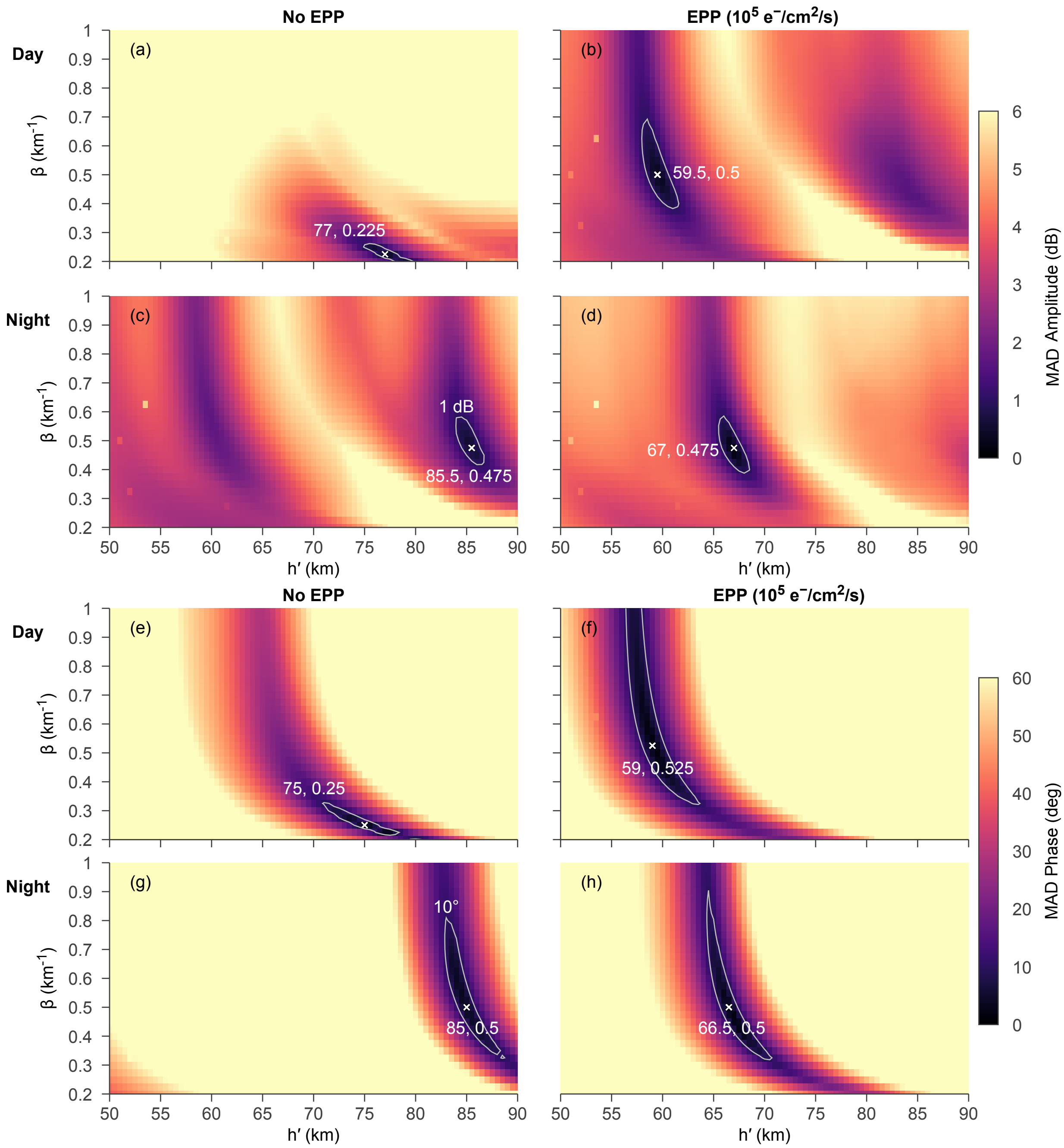

Figure 4. Mean absolute difference of the E_z amplitude (a–d) and phase (e–h) between Wait and Spies exponential ionospheres and a realistic undisturbed ionosphere (left) and EPP-perturbed ionosphere (right) along a 3000 km path. The precipitating electrons have an exponential energy distribution with $E_0 = 200$ keV and a constant flux of 10^5 e$^-$/cm^2/s. The white ×'s mark the h' and β parameters that result in the amplitude and phase curves most similar to the curve produced by the realistic ionosphere profile. Contour lines showing 1 dB amplitude and 10° phase difference are also drawn.

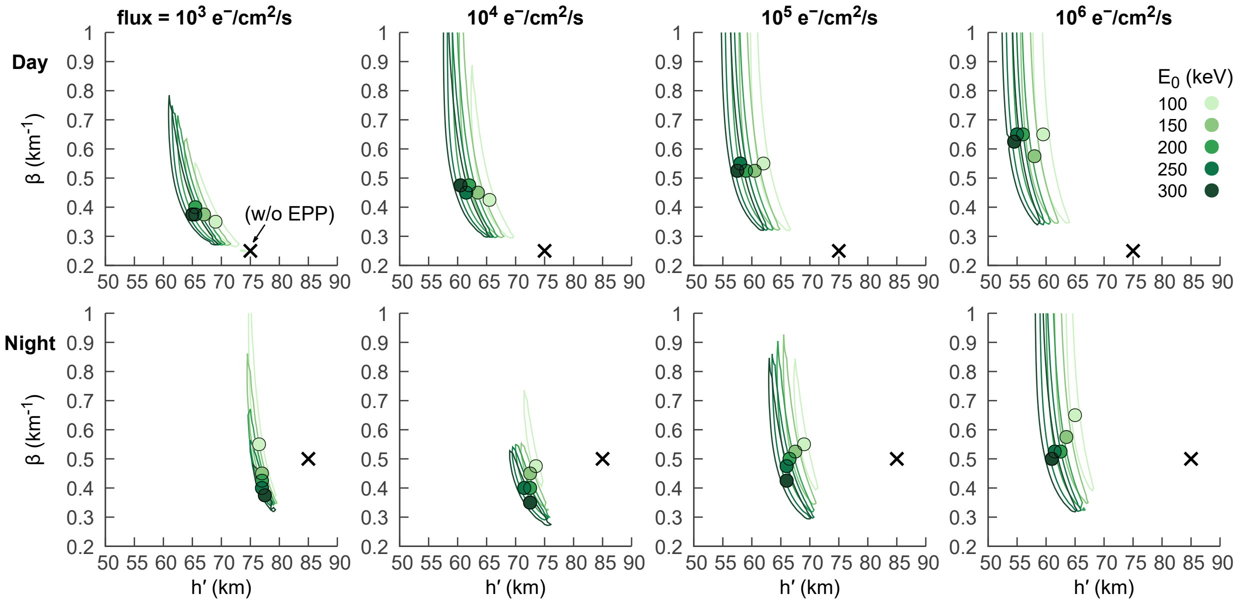

Figure 5. VLF phase-equivalent Wait and Spies ionospheres for a variety of EPP fluxes and energy distributions. The ∘ symbols mark the h', β MAD fit of each EPP ionosphere and are surrounded by 10° phase contours. The × symbol indicates the MAD fit of the undisturbed ionosphere. Local day is 2020-03-01 2000Z and night is 2020-03-02 0500Z.

$0.6\,\text{km}^{-1}$ at the 24 kHz transmitter frequency used to produce this figure. High β values represent rapid increases in electron density with altitude, trending towards a sharp waveguide boundary between free space below and the ionosphere above. Because the Wait ionosphere profile is exponential, higher β values have decreasing influence on the slope of the electron density, so a change from $\beta = 0.25\,\text{km}^{-1}$ to $\beta = 0.35\,\text{km}^{-1}$ is more significant than a change from $\beta = 0.55\,\text{km}^{-1}$ to $\beta = 0.65\,\text{km}^{-1}$.

This simulation and MAD calculation process was repeated for daytime and nighttime with several combinations of precipitating electron flux and energy distribution. The resulting best-fit exponential ionospheres and phase difference contours are shown in Fig. 5. Increasing flux is correlated with a decrease in h' relative to the undisturbed ionosphere, which is marked by × on the plot. Increasing flux is also correlated with an increase in β, but this effect is stronger in daytime than nighttime. The EPP ionospheres have a β of approximately $0.35\,\text{km}^{-1}$ or higher, which is greater than some typical daytime ionospheres. There is a weak correlation between higher E_0 values and lower h' ionospheres, but this trend does not extend to the nighttime ionosphere when there is low precipitating flux. Although there is also a trend between increasing E_0 and decreasing β at nighttime, the low sensitivity of the VLF observations to β may make E_0 difficult to retrieve in real data.

Realistic electron density profiles for daytime and nighttime are plotted in Fig. 6 with their corresponding exponential Wait profiles found by the best-fit phase MAD. Each daytime exponential profile accurately captures the electron density of their realistic profile from the base of the ionosphere up to the reflection height. The exponential profiles are plotted with dashed lines above the altitude at which Wait's conductivity parameter ω_r is equal to the angular transmitter frequency ω (Wait & Spies, 1964). This approximates the altitude at which the bulk of the wave reflection occurs (Ratcliffe, 1959). VLF observations have limited sensitivity to the ionosphere above this height and therefore we cannot estimate the ionosphere profile above this height. The nighttime expo-

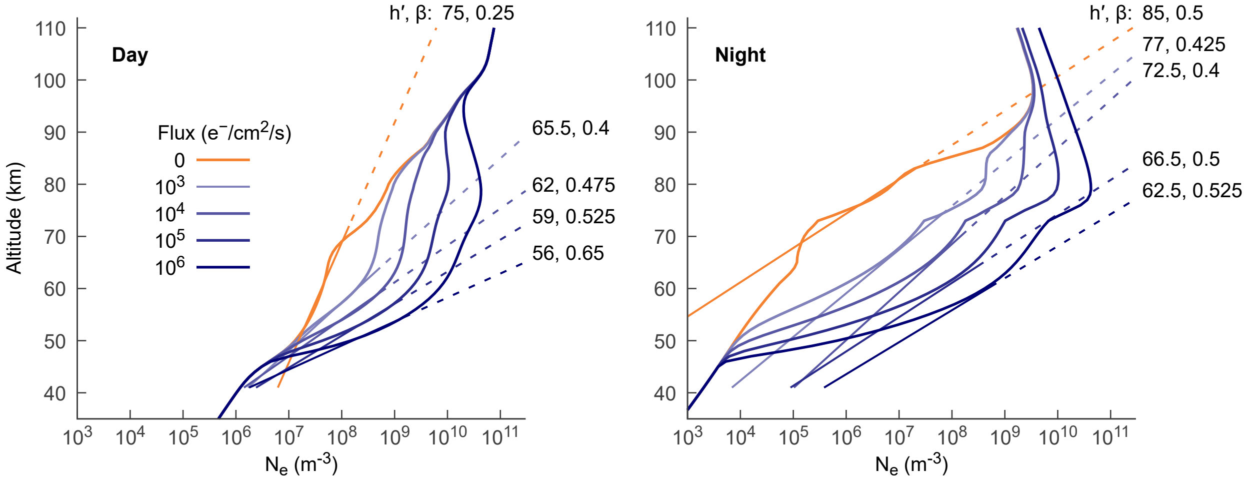

Figure 6. Realistic electron density profiles (curves) simulated using the process shown in Fig. 3 and the best-fit Wait profiles (lines) found from the MAD E_z phase along a 3000 km propagation path. Daytime ionospheres are shown on the left and nighttime are shown on the right. The Wait profiles are labeled with their h', β values and are dashed above the approximate reflection height at which $\omega_r = \omega$ (Wait & Spies, 1964).

nential profiles best fit the true profile just below the reflection height. A different ionosphere model than the Wait profile would be required to simultaneously fit the lower nighttime ionosphere and the altitudes near the reflection height.

The presence of EPP has a significant effect on the best-fit h' in Fig. 6. Lower levels of precipitation with a flux of $10^3\,\mathrm{e}^-/\mathrm{cm}^2/\mathrm{s}$ decreases h' by about 10 km from the undisturbed ionosphere. Strong precipitation with a flux of $10^6\,\mathrm{e}^-/\mathrm{cm}^2/\mathrm{s}$ decreases h' by 19 km in day and 24 km at night. In fact, the best-fit $h' = 62$ km retrieved at night would be low for a typical *daytime* ionosphere. Any VLF inversion method used to estimate an EPP-disturbed ionosphere must consider this large range of h' and β parameters. This is challenging because of the nonlinear relationship between the ionosphere parameters and the forward model "observation." Figure 4 shows there can be multiple minima even when the ionosphere parameters are constant along the propagation path and the signal amplitude is sampled every 5 km along the path. D-region estimation with real data often only has a single receiver measurement on each path and estimation of a segmented ionosphere significantly increases the parameter space. For example, a brute force estimate of a single 1000 km propagation path with five 200 km segments using the Wait parameter grid from Fig. 4 could require up to $\mathcal{O}(10^{15})$ forward model runs.

3.2 Precipitation Patch

In this section we look at VLF amplitude and phase with propagation through a localized region of EPP. Using the model shown in Fig. 3, we construct the segmented propagation paths by varying the precipitating flux as a function of geographic latitude and longitude. The precipitation patch used in this section is shown in Fig. 7. The patch flux F at longitude λ and latitude ϕ is defined by a two-dimensional super-Gaussian with a flat peak of flux p:

$$F(\lambda, \phi) = p \exp\left(-\left(a(\lambda-\lambda_0)^2 + 2b(\lambda-\lambda_0)(\phi-\phi_0) + c(\phi-\phi_0)^2\right)^n\right) \tag{4}$$

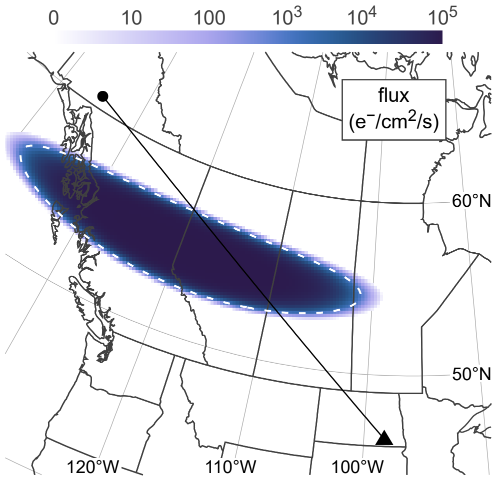

Figure 7. A precipitation region modeled as a two-dimensional super-Gaussian having a peak flux of 10^5 e$^-$/cm^2/s. The white dashed line contours a flux of 10^3 e$^-$/cm^2/s. The propagation path shown is from the NML transmitter in LaMoure, North Dakota to a receiver in Whitehorse, Yukon.

where

$$a = \cos^2\theta/(2\sigma_\lambda^2) + \sin^2\theta/(2\sigma_\phi^2) \tag{5}$$
$$b = -\sin(2\theta)/(4\sigma_\lambda^2) + \sin(2\theta)/(4\sigma_\phi^2) \tag{6}$$
$$c = \sin^2\theta/(2\sigma_\lambda^2) + \cos^2/(2\sigma_\phi^2) \tag{7}$$

and power $n = 4$, $\lambda_0 = 120^\circ\,\mathrm{W}$, $\phi_0 = 55^\circ\,\mathrm{N}$, $\sigma_\lambda = 11^\circ$, $\sigma_\phi = 1.3^\circ$, and $\theta = 1.5^\circ$.

Figure 8 shows the E_z signal amplitude and phase along the ground between the NML transmitter in LaMoure, North Dakota and Whitehorse, Yukon. The patch shape remains the same while the peak flux and energy distribution is varied. When the precipitation occurs during daytime there is a small, but measurable, change in amplitude, and the change in phase is a minimum of 5 times the typical phase noise of approximately 1°. During nighttime, there is a significant change in both amplitude and phase. This corresponds with the relatively larger $\Delta h'$ for precipitation at night seen in Section 3.1.

In general, the magnitude of precipitating flux has a much larger influence on the amplitude and phase curves than the precipitating energy distribution, i.e. E_0. The curves of identical precipitating flux are usually grouped together in Fig. 8, but there are several regions along the path at which the amplitude and/or phase curves cross one another. Even if the shape of the precipitation patch were known, it would be difficult to separate precipitating energy distribution and flux in a retrieval from a real VLF receiver if it happens to be located in one of these regions. An array of distributed receivers is likely to include amplitude and phase measurements that are outside of these regions and distinctly associated with a magnitude of precipitating flux. In practice, the simultaneous fit of receiver array observations generates an ionosphere estimate that balances the size, shape, energy, and intensity of precipitation (see Section 4).

4 Ionosphere Imaging Methodology

An array of geographically distributed VLF transmitters and receivers can be used to image the spatial extent of an EPP patch. Each propagation path in a VLF array observes a unique "slice" through the observation region, which may intersect a precipi-

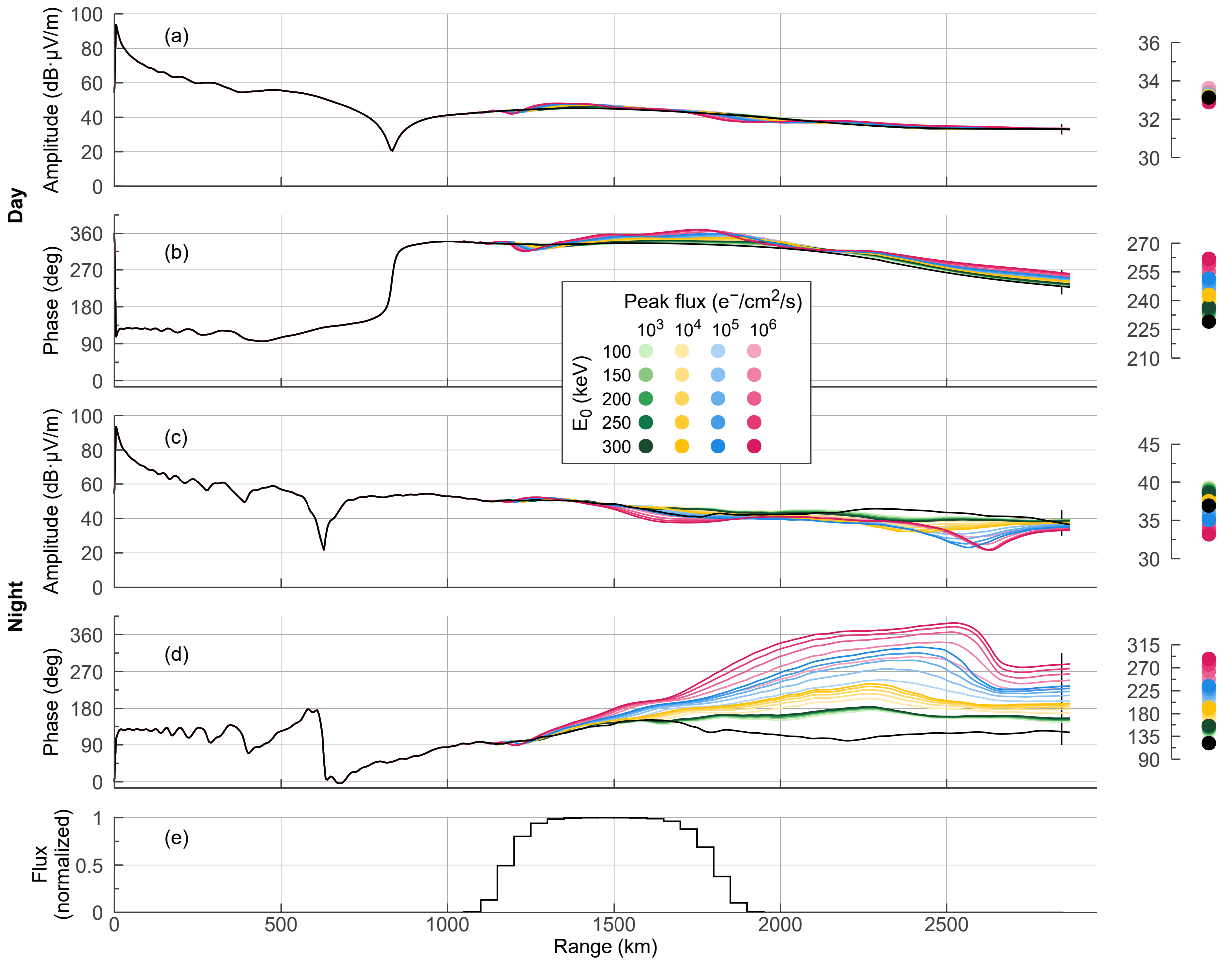

Figure 8. Signal amplitude (a, c) and phase (b, d) curves along the path from the NML transmitter to Whitehorse, Yukon for the propagation path shown in Fig. 7. EPP with several different fluxes and energy distributions E_0 are shown in color over a daytime (a, b) and nighttime (c, d) background ionosphere. Curves without EPP are shown in black. Subfigure (e) is a normalized trace of the precipitating flux along the propagation path.

tation patch. The full set of propagation paths used in this work is shown in Fig. 9 (c) and (d). The goal of the imaging algorithm is to combine the information from each slice to produce a continuous estimate of the spatially varying ionosphere across the region. The retrieved ionosphere should be consistent with all of the receiver observations and have a reasonably realistic spatial correlation.

Imaging of the D-region ionosphere using VLF signals is an ill-posed, nonlinear inverse problem. To solve it we apply an ensemble Kalman filter (EnKF) algorithm called the local ensemble transform Kalman filter (LETKF) (Hunt et al., 2007). This algorithm was previously presented as a method to estimate undisturbed ionospheres (Gasdia & Marshall, 2019), but a brief overview will be given here. In this work we use an ensemble of $k = 100$ ionospheres $\boldsymbol{x}_b$ that statistically represent the best estimate of the true ionosphere prior to any observations being made. The covariance matrix of the ensemble of prior ionospheres is $\boldsymbol{P}_b$ where subscript b indicates "prior". The Kalman filter compares real, noisy receiver observations $\boldsymbol{y}_o$ to LWPC model "observations" $\boldsymbol{y} = \mathcal{H}(\boldsymbol{x})$ using the ensemble ionospheres. Under the assumption that the system can be modeled with a multivariate Gaussian distribution, the ensemble is adjusted to reduce the measurement residuals according to the relative uncertainty between the prior estimate and the measurement noise. If $\boldsymbol{X}_b$ and $\boldsymbol{Y}_b$ are the zero-mean vectors $\boldsymbol{x}_b - \overline{\boldsymbol{x}_b}$ and $\boldsymbol{y}_b - \overline{\boldsymbol{y}_b}$, and the measurement noise covariance is $\boldsymbol{R}$, then the LETKF estimate for the ionosphere $\boldsymbol{x}_a$ with covariance $\boldsymbol{P}_a$ after assimilating observations from the receiver array is

$$\boldsymbol{x}_a = \boldsymbol{x}_b + \boldsymbol{X}_b \tilde{\boldsymbol{P}}_a \boldsymbol{Y}_b^\top \boldsymbol{R}^{-1} (\boldsymbol{y}_o - \mathcal{H}(\boldsymbol{x}_b)) \tag{8}$$

$$\tilde{\boldsymbol{P}}_a = \left((k-1)\boldsymbol{I} + \boldsymbol{Y}_b^\top \boldsymbol{R}^{-1} \boldsymbol{Y}_b\right)^{-1} \tag{9}$$

$$\boldsymbol{P}_a = \boldsymbol{X}_b \tilde{\boldsymbol{P}}_a \boldsymbol{X}_b^\top . \tag{10}$$

The LETKF can also step the state estimate and covariance through time, but this would require a forecast model describing the time dynamics of both the undisturbed ionosphere and an unknown disturbance, such as EPP. Instead, this work iterates the measurement update over a series of noisy array observations to converge to a solution. To prevent the filter from becoming overconfident, the estimate covariance is inflated by 10% at each iteration.

The state of the ionosphere is represented by a flattened vector of h' and β values defined at points across a geographic map. Unlike in Gasdia and Marshall (2019), the points are defined as a grid with 300 km spacing on the North America equidistant conic projection plane known as ESRI:102010. This projection preserves distance between the grid points along all meridians and along the 20° N and 60° N parallels. Other projections could have been chosen; the intent is to distribute the grid points more uniformly than if they were defined on a grid of geographic latitude and longitude. For input to LWPC, h' and β values are interpolated from the grid points onto the propagation paths using a first order polynomial interpolator (Ljungskog, 2021). The interpolator is also used to produce an estimated ionosphere map at high resolution. Additional discussion of this technique is given in Gasdia (2021). To localize the influence of receiver measurements on the ionosphere estimate, grid points are only updated using propagation paths that pass within 600 km. Therefore, grid points near the edge of the map are updated using only a couple of observations, while grid points near the center of the map use a large number of observations.

The LETKF requires computation of the pre-fit residual amplitude and phase for each propagation path, $\boldsymbol{y}_o - \mathcal{H}(\boldsymbol{x}_b)$. To meaningfully calculate the difference between real receiver measurements and the LWPC forward model, the model and receivers must be calibrated so that if the true conditions in the Earth-ionosphere waveguide were perfectly known, there would be no difference between the model and the measurements. In practice this is a challenging requirement for several reasons: we have imperfect knowledge of the waveguide parameters, the forward model has limited resolution and makes simplifying assumptions about the physics of propagation, and we have limited information about the VLF transmitters. However, we are actively investigating techniques to calibrate VLF measurements. The receivers can be cross-calibrated to have the same relative amplitude response and GPS time signals allow all of them to be synchronized in phase. The receivers are placed in remote areas away from man-made interference, and we can measure the transmitted phase by placing an additional reference receiver close to each transmitter. Recent models for Earth's magnetic field, such as CHAOS (Finlay et al., 2020), are sufficiently accurate that they no longer introduce significant error into the forward model during undisturbed conditions (Gasdia, 2021). Analysis of stable daytime data on each path may enable correction of constant biases due to errors in the ground conductivity map. There are multiple physical phenomena that cause variablility in VLF propagation besides EPP, particularly at nighttime. Demirkol et al. (1999) correlated the effect of nighttime EPP on VLF propagation with satellite-borne energetic electron detectors, and to reduce the influence of other phenomena they averaged the VLF signal amplitude over three-hour intervals. Similar data averaging could be applied before assimilation with the LETKF, especially to remove nighttime flutter.

Estimating an EPP-disturbed ionosphere without prior knowledge that EPP is occurring is difficult and time consuming because of the size of the parameter space that must be considered (see Section 3). The prior estimate of the ionosphere must be sufficiently close to the truth that the assumptions under which the LETKF ensemble update was derived are not strongly violated. If the state and measurement noise distributions are highly non-Gaussian or the system too nonlinear, then the ensemble adjustment may not decrease the measurement residuals and the ensemble estimate will diverge. In practice, VLF receiver arrays continuously record transmitter signals, so an estimate of the undisturbed ionosphere can be made before precipitation begins. This estimate is already close to the truth across much of the region at the onset of a precipitation event. The filter is more likely to converge to the correct estimate of the disturbed region if the pre-precipitation estimate is used as the prior. Although in Section 5 we only use a single pre-precipitation estimate as the prior for an ionosphere perturbed by moderate precipitating flux, future work could make estimates in small time steps as the ionosphere is perturbed more and more from the initial background.

5 Simulated Observation Experiments

This section uses simulated VLF observations to demonstrate D-region imaging with an array of VLF transmitters and receivers. The simulation includes 11 receivers across the western half of Canada with amplitude and phase observations of both the NML (25.2 kHz) and NLK (24.8 kHz) transmitters in LaMoure, North Dakota and near Oso, Washington. Each estimate assimilates six noisy observations and iterates over the LETKF measurement update. Simulated receiver observations are generated using the LMP propagation model. Not only does LMP include electrons and the four ion density profiles output from GPI, but Gaussian noise with a standard deviation of 0.1 dB in amplitude and 1° in phase is added to each observation to simulate realistic receiver measurement noise. It may be necessary to adjust these values to model the noise from real individual receivers, but in our experience these values are typical of daytime observations. Nighttime data is much more variable, but through temporal averaging it may be reduced to these levels. LWPC is used as the forward model $\mathcal{H}$ in the LETKF estimate and assumes an electrons-only Wait and Spies exponential ionosphere parameterized by h' and β.

5.1 Exponential Daytime Ionosphere

This scenario simulates the truth ionosphere as a geographically-varying Wait and Spies exponential ionosphere. This is the only scenario presented in this article in which the state estimate can perfectly capture the true ionosphere and the state estimate error can be directly quantified. This is because we are estimating the ionosphere as parameterized by h' and β, but the simulations later in this section use a realistic profile that is not defined as a Wait ionosphere profile. Therefore, although we know the truth in all of these simulations, this is the only one in which the estimated ionosphere and truth ionosphere are both defined by h' and β and we can calculate the difference between them.

The geographic variation in this simulation's truth ionosphere is defined by a Fourier disturbance on top of an ionosphere model presented by Ferguson (1980):

$$h'_{\mathrm{F}}(\phi,\chi,m) = 74.37 - 8.097\cos\chi + 5.779\cos\phi - 1.213\cos(2\pi(m-0.5)/12) \quad (11)$$

$$\beta_{\mathrm{F}}(\phi,\chi,m) = 0.3849 - 0.1658\cos\chi - 0.08584\cos\phi + 0.1296\cos(2\pi(m-0.5)/12) \quad (12)$$

$$h'_{\mathrm{d}}(\chi) = 2.35 + 0.98\cos(8\chi) - 0.17\cos(16\chi) - 0.28\sin(8\chi) + 0.1\sin(16\chi) \quad (13)$$

$$\beta_{\mathrm{d}}(\chi) = 0.03 + 0.01\cos(8\chi) + 0.008\cos(16\chi) - 0.002\sin(8\chi) - 0.008\sin(16\chi) \quad (14)$$

$$h'_{\mathrm{true}}(\phi,\chi,m) = h'_{\mathrm{F}}(\phi,\chi,m) + h'_{\mathrm{d}}(\chi) \quad (15)$$

$$\beta_{\mathrm{true}}(\phi,\chi,m) = \beta_{\mathrm{F}}(\phi,\chi,m) + \beta_{\mathrm{d}}(\chi) \quad (16)$$

for geographic latitude ϕ, solar zenith angle χ, and month-of-the-year number m. These equations are used to compute h' and β every 50 km along each propagation path to build segmented waveguides for LMP to simulate real observations. They are also used to produce a map of the ionosphere for comparison with the estimated ionosphere.

The prior estimate for the undisturbed ionosphere used in this scenario and elsewhere in this work is the Ferguson ionosphere, described by Eqs. (11) and (12). The ensemble is generated by sampling from a multivariate Gaussian distribution with the Ferguson ionosphere as the mean and a standard deviation of 2 km in h' and $0.04\,\mathrm{km}^{-1}$ in β. Additionally, the covariance matrix has a Gaussian-like spatial correlation with a length-scale of 600 km, independent between h' and β (Gaspari & Cohn, 1999). This provides unique spatial structure in each ionosphere of the ensemble. See Gasdia and Marshall (2019) for additional details.

Figure 9 shows the error in the prior and VLF-estimated ionospheres. The prior h' and β are both biased low across the region and also have some variability across latitude. The estimate removes the overall bias, but the h' map has localized regions of higher error. The β estimate has low error across the map. Some of this difference is due to the use of two different propagation models, LMP and LWPC, to generate simulated truth measurements and LETKF forward model observations. In particular, LMP includes 4 ion species when LWPC assumes an electrons-only ionosphere. This will drive a slight difference between the estimated and truth ionospheres, even if the forward model runs match the simulated truth observations.

Figure 10 shows residuals between the modeled and "true" amplitude and phase observations for each iteration of the LETKF. Each circle ($\circ$) represents the measurement residual for a single propagation path. Iteration 0 is the difference between the observations modeled with the prior ionosphere and the first observation. All other iterations have post-fit residuals such that iteration 6 is the difference between the observations modeled with the estimate after six iterations of the LETKF and the sixth "real" observation. By the third iteration of the LETKF, both the amplitude and phase residuals are within about 2σ of the measurement noise, meaning the filter estimate is consistent with the observations down to the Gaussian noise that was added to the simulated truth observations. This same analysis can be performed with real data, when the truth is unknown, to determine if the real observations can be reproduced with the estimated ionosphere.

5.2 Realistic Daytime Ionosphere

The first step to imaging an EPP precipitation patch is to estimate the undisturbed ionosphere before precipitation begins. This estimate is then used as the prior estimate

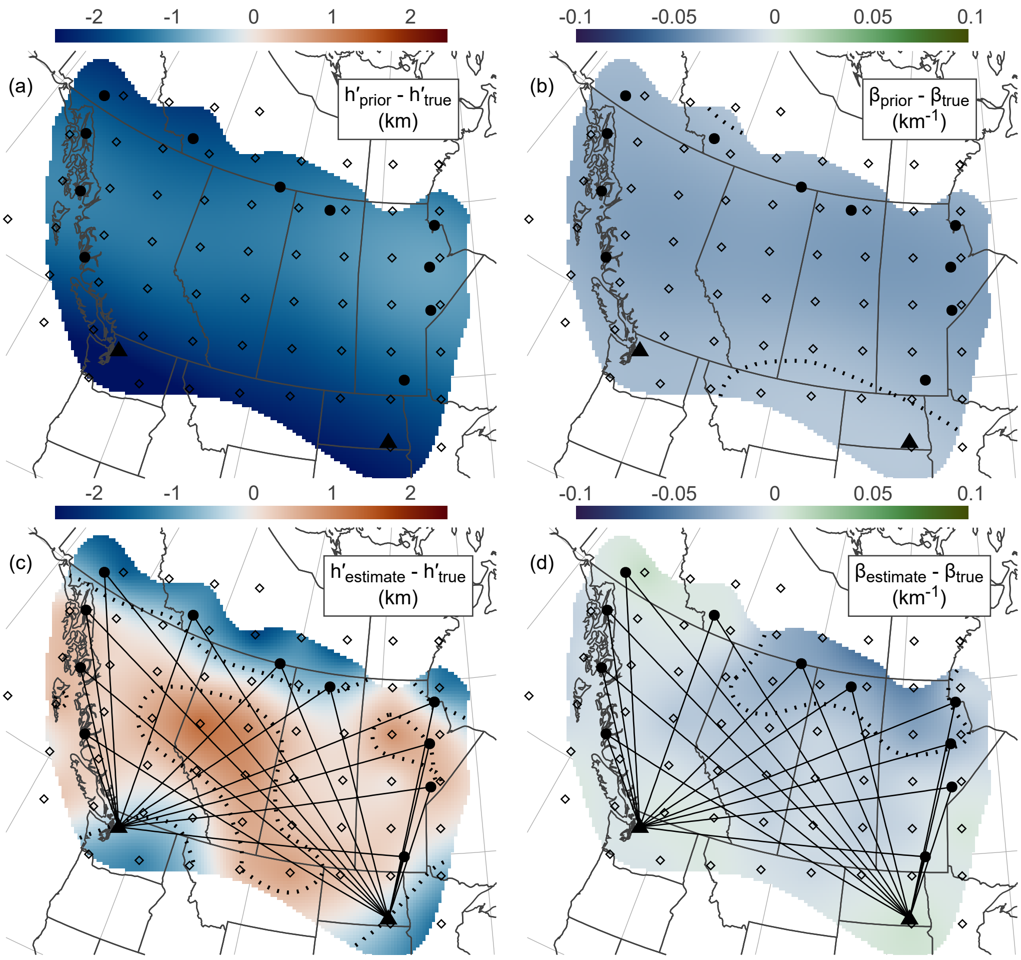

Figure 9. Top: difference between the prior and true ionosphere h' (a) and β (b) when the truth is defined using Wait's exponential ionosphere profile. Dotted lines on the error maps are 0.5 km h' and 0.05 km^{-1} β contours. Bottom: error in the LETKF estimated ionosphere. The black lines crisscrossing the map represent each of the VLF propagation paths from transmitters (▲) to receivers (●) with observations assimilated into the LETKF. The open diamonds (◇) are the geographic points at which h' and β values are specified. The rest of the map is constructed by interpolation between those points.

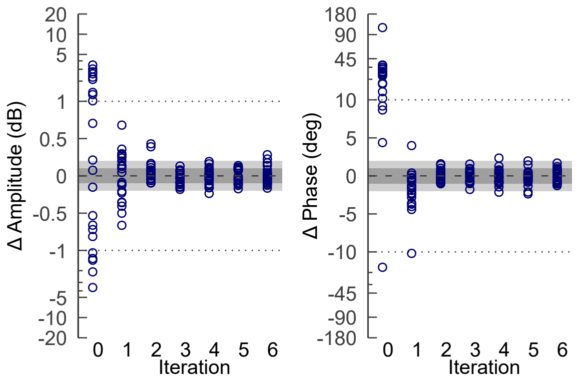

Figure 10. Signal amplitude (left) and phase (right) residuals between model observations of the estimated ionospheres and simulated truth observations for each propagation path using the daytime Wait and Spies truth ionosphere. The vertical axis of both plots is linear inside the horizontal dotted lines and logarithmic outside to better display the wide range of values. The gray shaded regions represent $\pm 1\sigma$ and $\pm 2\sigma$ of typical measurement noise.

for data with a precipitation event. In this section we estimate an undisturbed daytime ionosphere at 2020-03-01 2000Z, but unlike the previous section, the simulated truth observations are generated using realistic ionosphere profiles from the process shown in Fig. 3. The LETKF estimate parameterizes the ionosphere using h' and β defined at grid points across the map. As such, it is not possible to quantify the error in the same way as Fig. 9, since there is no "truth" map in h' and β.

Beginning with the same Ferguson prior as used in Section 5.1 and iterating the LETKF over six noisy observations results in the estimate shown in Fig. 11. Both h' and β vary slowly across the map and have typical daytime values of about 77 km h' and 0.23 km^{-1} β. Although the propagation paths are not plotted on the maps, there is a difference in the estimate along the edge of the map, where information is provided by only one or two receivers, and the middle of the array, where the estimate must be consistent with several receiver observations. A map of the statistical confidence based on the state covariance would reflect this lower level of information around the edge of the map by showing greating uncertainty in the estimate there.

Plots of the true and estimated electron density profile at three locations across the map are shown in Fig. 12. The Wait and Spies estimate at all three locations is a close fit to the true profile between 50 km and 70 km altitude. The Wait profile is dashed in Fig. 12 above the height at which much of the wave reflection has occurred (Ratcliffe, 1959). It is not expected to be a close match to the true profile above this height, which is approximately 75 km in Fig. 12.

The h' and β ensemble distributions at those same locations numbered 1, 2, and 3, are plotted in Fig. 13. The prior ensemble was chosen to have a high standard deviation because there is a large uncertainty that the Ferguson ionosphere accurately represents the truth. The ensemble distribution narrows as observations are assimilated into the estimate by the LETKF, signifying greater confidence in the estimate. The ensemble distributions at location 3 are relatively wide compared to locations 1 and 2 because fewer propagation paths provide information to the measurement update there.

A more robust way of assessing the accuracy of the filter estimate is to examine the measurement residuals, shown in Fig. 14. As in the Wait and Spies exponential truth scenario, the residuals are within two standard deviations of both the amplitude and phase

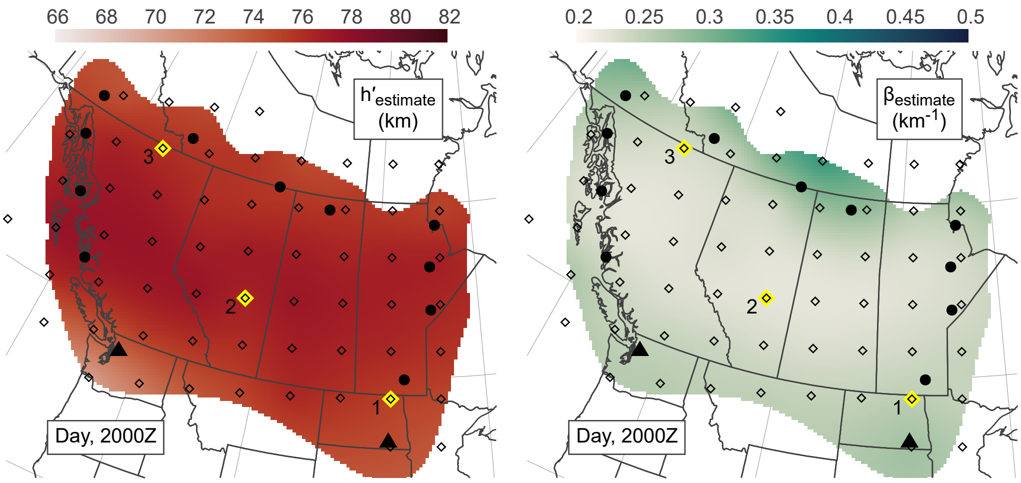

Figure 11. Realistic daytime ionosphere estimate after six LETKF iterations.

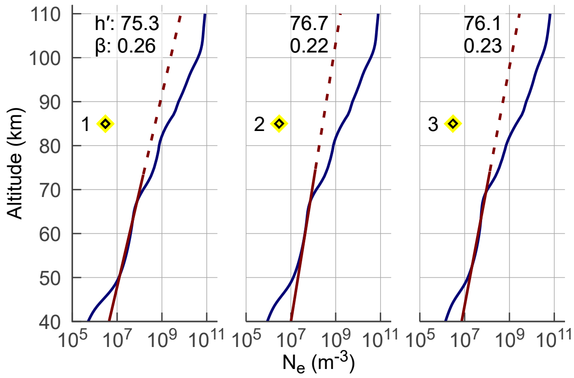

Figure 12. True and estimated (exponential) profiles at the locations labeled 1, 2, and 3 and highlighted yellow in Fig. 11. The estimated profiles are plotted with dashed lines above the approximate wave reflection height. The h' and β parameters of the estimated profiles are indicated at the top of each plot.

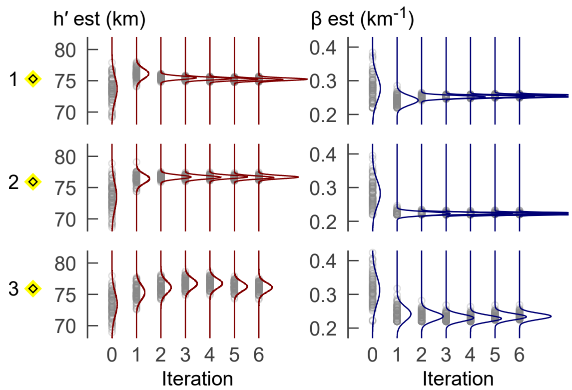

Figure 13. Ensemble distributions of h' (left) and β (right) at each iteration of the LETKF sampled at the locations marked 1, 2, and 3 in Fig. 11.

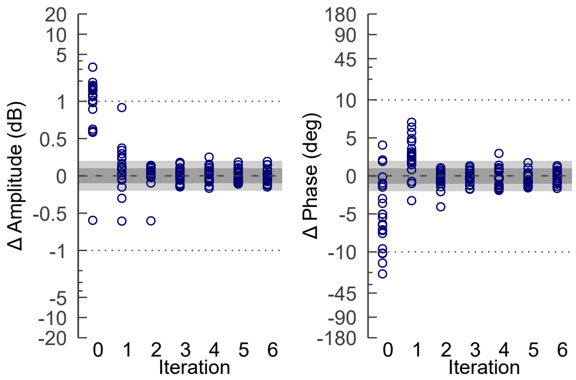

Figure 14. Measurement residuals between the estimated ionosphere model observations and simulated daytime truth observations at each iteration of the LETKF.

Table 1. Super-Gaussian parameters from Eq. (4) used to describe the daytime EPP patches in scenarios (a)–(d).

	Scenario			
	(a)	(b)	(c)	(d)
p (e$^-$/cm^2/s)	10^5	10^5	10^4	10^4
ϕ_0	55° N	55° N	58° N	52° N
λ_0	110° W	120° W	125° W	100° W
σ_ϕ	1.5°	1.3°	1.5°	0.6°
σ_λ	3°	11°	12°	6°
θ	0°	1.5°	−3°	0°

measurement noise by the third iteration of the filter. This demonstrates that the estimated ionosphere is consistent with the observations.

5.3 EPP-Disturbed Daytime Ionosphere

In this section we present four scenarios with EPP occurring in local daytime at 2020-03-01 2000Z. Each precipitation patch is modeled as a super-Gaussian (Eq. (4)) with parameters summarized in Table 1. All of the scenarios use precipitation with an exponential energy distribution having $E_0 = 200\,\text{keV}$. Truth ionosphere profiles are generated using the process described in Section 3.2. The LETKF prior ionosphere is the estimate of the nighttime ionosphere without EPP, shown in Fig. 11, and the filter has no *a priori* knowledge that EPP is occurring. The covariance matrix used to generate the ensemble is the same one used in Section 5.1 and Section 5.2.

The results of iterating the LETKF over six noisy array observations for each of the precipitation scenarios (a)–(d) are shown in Fig. 15. The dashed white line on the h' and β estimate maps is the true 10^3 e$^-$/cm^2/s precipitating flux contour for each scenario. In all four of the h' estimate maps, the h' estimate in the precipitation region is lower than the surrounding h' estimate, indicating the presence of a significant ionospheric disturbance in that location. Based on the results of Section 3.1, precipitating flux of 10^4 to 10^5 e$^-$/cm^2/s produces an ionosphere with an effective h' of about 60 km and an effective β of 0.5 km^{-1}. The LETKF estimate approaches this low h' value for the two largest precipitation patches in scenarios (b) and (c). The β estimates, however, show little structure that is consistent with a precipitation patch. Estimates for scenarios (b) and (c) may have a slight increase in β in the patch region, but there is variation of β across the map. This is at least partially explained by the relatively low sensitivity of subionospheric VLF observations to β, previously shown in Section 3.

Also shown in Fig. 15 are the true and estimated ionosphere profiles at three geographic locations for each of the precipitation scenarios. In every scenario, location 1 is outside of the precipitation region and the estimated profile is a good match to the true profile between at least 50 to 70 km altitude. In scenarios (a) and (b), location 2 is inside the precipitation region, and in scenario (c), location 3 is inside the precipitation region. Although the h' estimate maps indicate a disturbed ionosphere, the estimated exponential profiles are not a very good match to the true EPP-disturbed profiles. The profile mismatch is dominated by the difference between the estimated and "true" β, assuming that the estimated profile should fit the true profile between a number density of 10^7 and $10^9\,\mathrm{e^-/m^3}$, where it fit in Section 3.2. The scenario (c) location 3 estimate is closest to the true profile, but only just below the reflection height at 60 km.

Measurement residuals for each of the precipitation scenarios are shown in Fig. 16. The residuals decrease with each iteration, but unlike the estimates made in Sections 5.1 and 5.2, none of the estimates result in both amplitude and phase residuals fitting the measurement noise level. This suggests there is some error in the estimates, which is consistent with the maps shown in Fig. 15. Although it may be possible to run the LETKF for additional iterations, the filter diverged for scenario (b) after only 5 iterations. This may have been the result of the filter estimate becoming statistically overconfident relative to the magnitude of the measurement residuals, or one of the ensemble ionospheres may not have been suitable for LWPC. Underestimation of the state covariance by ensemble Kalman filters is an active research area, but may be improved in future work by implementing additive covariance inflation between iterations or cross validation of the ensemble members in the LETKF measurement update (Houtekamer & Zhang, 2016; Buehner, 2020). If LWPC is the problem, it could be replaced with LMP as the LETKF forward model because LMP is more robust to atypical ionosphere profiles.

5.4 Realistic Nighttime Ionosphere

This section is the nighttime counterpart to Section 5.2. Realistic ionosphere profiles are generated for 2020-03-02 0500Z and no EPP is present. The prior ionosphere is the Ferguson model and the same covariance is used to generate the ensemble members as in the other simulated observation experiments. The h' and β estimate maps after iterating the LETKF over six array observations are shown in Fig. 17.

Unlike the daytime estimate, the nighttime estimate maps for h' and β have a significant amount of spatial structure and variation. The truth profiles were generated using the process shown in Fig. 3 and include no other disturbances, so the estimate maps should have very little variation. Instead, the h' estimate ranges from 76 to 95 km and the β estimate ranges from 0.27 to $0.7\,\mathrm{km^{-1}}$. Additionally, the spatial structure between the h' and β maps is not correlated.

If this estimate were produced using real measurements and the true state of the ionosphere was unknown, the measurement residuals would be used to validate the estimate. Residuals for this scenario are shown in Fig. 18. The residuals at the final iteration are well outside of the measurement noise, indicating that the final estimate is not a good fit to the observations. In fact, the residuals improve very little at each iteration. The LETKF updates did not move the ensemble much closer to the true ionosphere. Similarly poor estimates were obtained when the simulated truth observations were generated for different times throughout the night. Estimates made for additional realistic nighttime ionospheres are shown in Appendix A. The high residuals associated with these undisturbed nighttime estimates makes them unsuitable as a prior for estimating EPP at night-

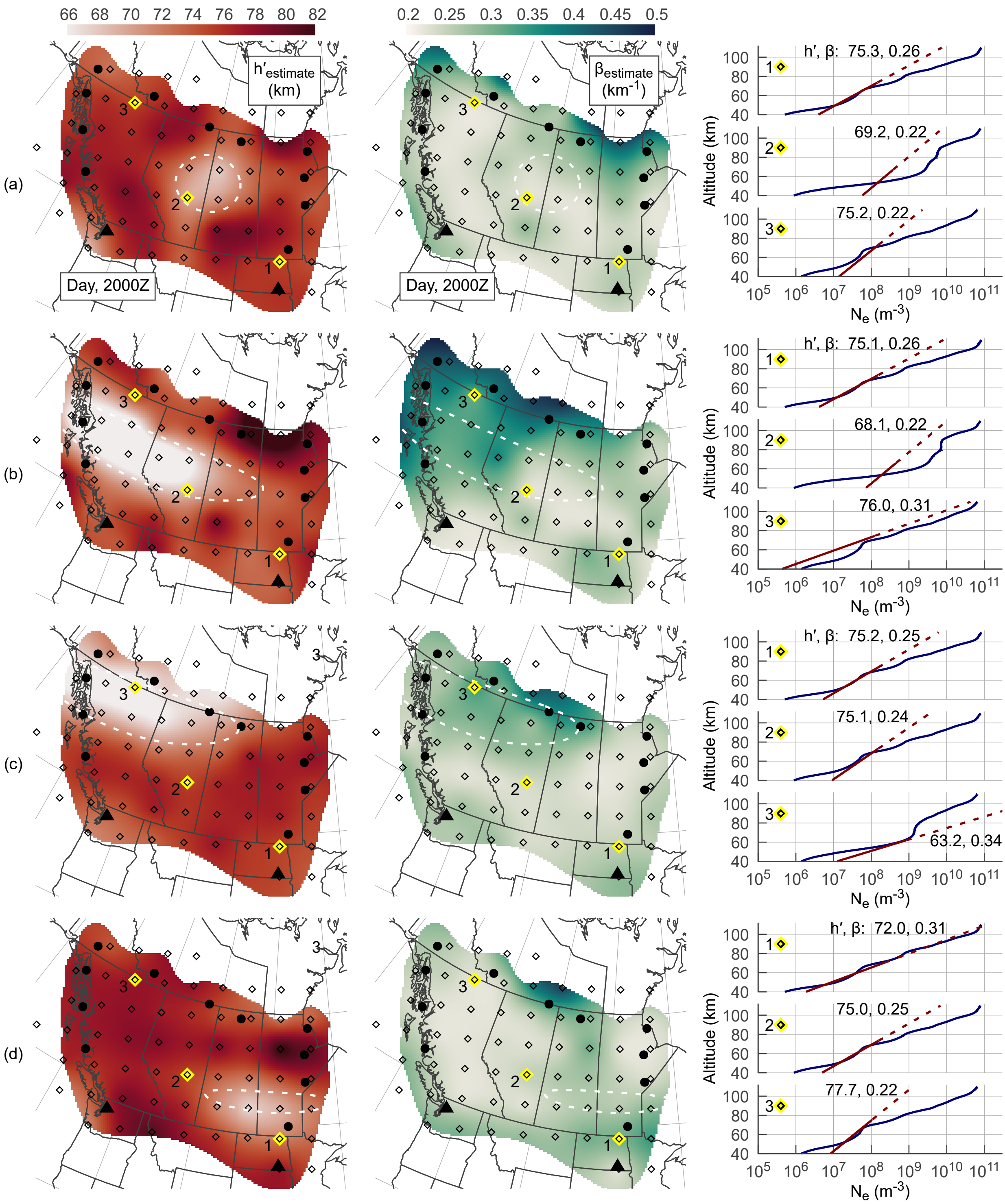

Figure 15. Estimated ionosphere h' (left column) and β (middle column) for 4 different EPP patches labeled (a) through (d). The $10^3\,e^-/cm^2/s$ precipitating flux contour is traced with a dashed white line. The right column shows the true electron density in blue and estimated profile in red at the points labeled 1, 2, and 3 and highlighted yellow on the maps.

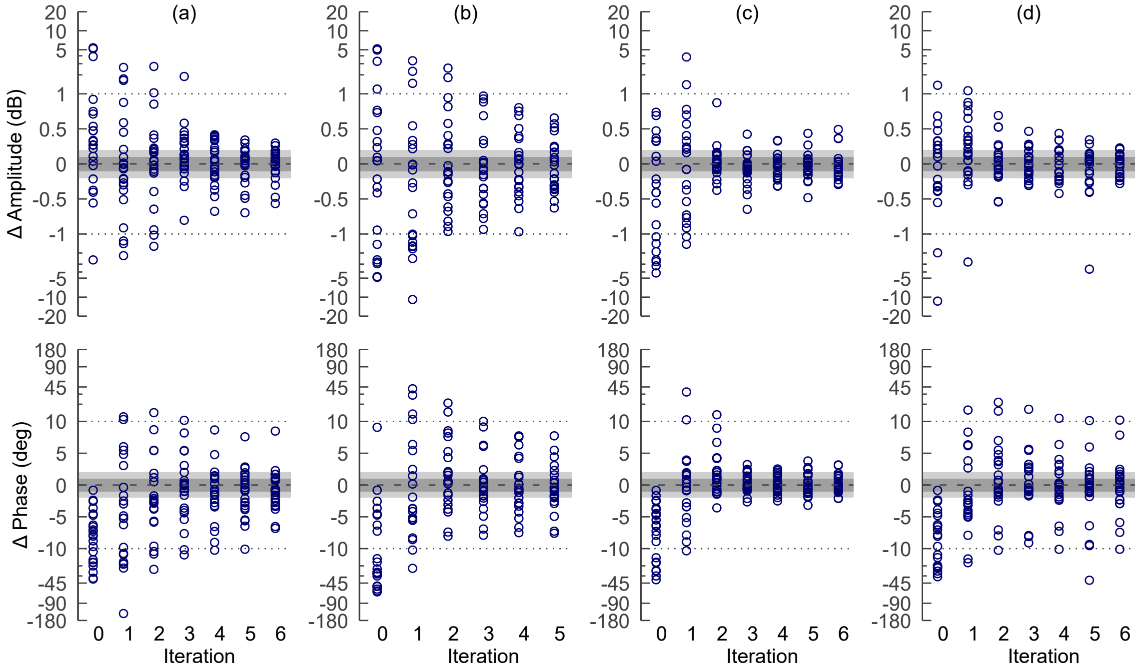

Figure 16. Signal amplitude (top) and phase (bottom) residuals between the estimated ionosphere model observations and simulated truth observations at each iteration of the LETKF. Columns (a)–(d) correspond to precipitation scenarios (a)–(d).

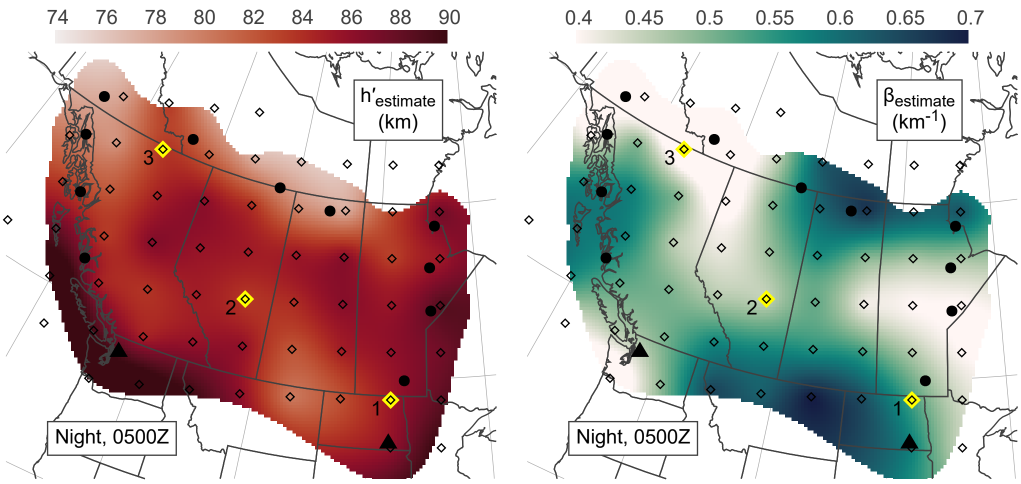

Figure 17. Estimated h' (left) and β (right) after six LETKF iterations over observations simulated with a realistic nighttime ionosphere.

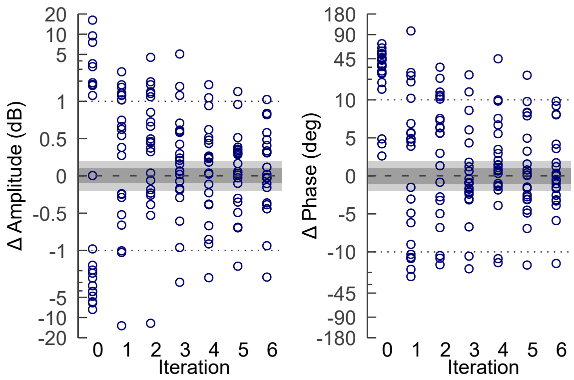

Figure 18. Measurement residuals between the estimated ionosphere model observations and simulated nighttime truth observations at each iteration of the LETKF.

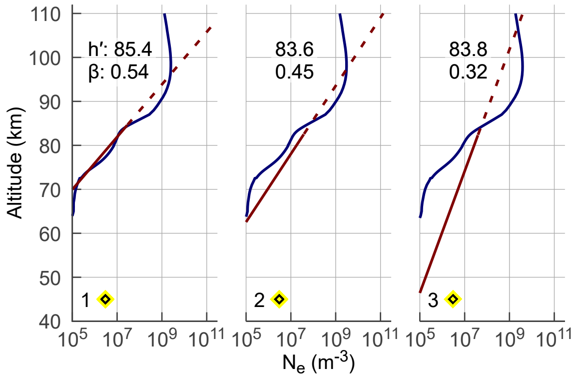

Figure 19. True electron density profile in blue and Wait exponential ionosphere estimates in red at locations 1, 2, and 3 marked with yellow diamonds in Fig. 17.

time. Although not shown, the LETKF frequently diverged at the first or second iteration for nighttime EPP scenarios.

Figure 19 shows the true and estimated ionosphere profiles at the three locations marked 1, 2, and 3 on Fig. 17. The true nighttime profile is significantly different from the daytime profile. Whereas the daytime profile is approximately exponential between 10^7 and 10^8 e^-/m^3 at 50 to 70 km altitude, the nighttime profile has a sharp knee at 10^7 e^-/m^3. The LETKF estimate is attempting to fit the nighttime profile between 10^5 and 10^7 e^-/m^3. This region of the profile has some structure, but is roughly fit by an exponential with a β of 0.5 km^{-1}, which is approximately the mean of the prior ionosphere. Because the prior ensemble is generated with a standard deviation of $\sigma_\beta = 0.04$ km^{-1}, the β estimate is weighted towards staying near 0.5 km^{-1}. The slope of the true profile between 10^7 and 10^9 e^-/m^3 has a β of about 1 km^{-1}. This is too many standard deviations away from the prior ensemble distribution for the filter to consider.

In a separate experiment (see Appendix B), we adjusted the prior so that h' used the Ferguson model, Eq. (11), but β used a mean of 0.9 km^{-1}. The estimate generated using this alternative prior was no better than the fully Ferguson prior. The β estimate decreased from 0.9 km^{-1} to about 0.5 km^{-1} across much of the map. This suggests that the exponential Wait and Spies profile may not sufficiently capture the true ionosphere profile as observed by subionospheric VLF signals. Future work should consider exploring the feasibility of representing the ionosphere profile with a higher fidelity model, such as the four-parameter models of McCormick and Cohen (2021) or Xu et al. (2021) to provide better fits.

6 Conclusions

In this article we have simulated the subionospheric propagation of narrowband VLF signals through ionospheres disturbed by energetic particle precipitation (EPP). High precipitating flux can significantly lower the effective height of the D-region ionosphere. When fit to an exponential Wait ionosphere profile, the h' of an ionosphere disturbed by EPP can decrease by 20 km compared to the undisturbed ionosphere. Fits of VLF amplitude and phase between realistic ionospheres disturbed by EPP and Wait ionospheres suggest that it may be possible to identify the magnitude of precipitating flux but not the energy distribution. We have applied the local ensemble transform Kalman filter (LETKF) to image four simulated EPP patches with a distributed array of VLF receivers. This method shows promise for identifying the presence and spatial extent of particle precipitation in daytime. This is primarily indicated by the estimation of regions with significantly perturbed h'. The estimated β maps do not strongly correlate with regions of precipitation. Although we only explored four precipitation scenarios, the estimates did not clearly retrieve the two different precipitating flux levels that were used across the scenarios. This is likely because the inversion problem is underdetermined and the retrieval balances the size of the precipitation region with the degree of disturbance. Nonetheless, application of the LETKF technique to real VLF array data could be used to automatically determine when and where energetic particle precipitation is occurring. We used an estimate of the undisturbed ionosphere as the prior for an estimate with moderate precipitating flux, but future work could estimate the ionosphere in several steps as the precipitating flux increases from the background. This would result in the filter making smaller adjustments to the estimate update and remain closer to the linear process assumptions under which the Kalman filter was originally derived.

Estimation of the Wait and Spies parameters for nighttime ionospheres is challenging using narrowband subionospheric VLF signals. VLF observations are less sensitive to the high β, rapid increases in electron density with altitude that are typical of nighttime ionospheres. Additionally, nighttime ionosphere profiles have structure that are not well captured by a single exponential Wait and Spies profile. Higher fidelity representations of the estimated ionosphere and temporal averaging of VLF receiver measurements should be considered to improve estimation of the nighttime D-region. Application of the LETKF to real data is further complicated by the requirement that the forward model be calibrated to the measurements. The receiver array must be referenced to the transmitter signal amplitude and phase. Errors in the ground conductivity map and magnetic field model also corrupt the estimate. In future experiments to test this methodology, we plan to overcome these challenges by placing reference receivers nearby the transmitters and by incorporating high fidelity auxiliary models into the forward propagation model. The approach taken in this work to simulate realistic ionosphere profiles begins to demonstrate a procedure that could be used to generate a realistic prior, or be used by the forward model when estimating with real data.

Appendix A Additional nighttime estimates

Section 5.4 applied the LETKF to observations simulated for a typical undisturbed ionosphere at 2020-03-02 0500Z, early nighttime on the west coast of British Columbia. The measurement residuals of the estimate are above the measurement noise and the estimated h' and β maps exhibit significant spatial variation. This section presents the results of applying the LETKF to observations simulated at two different times of night: (a) 2020-03-02 0800Z, midnight on the west coast, and (b) 2020-03-02 1100Z. The es-

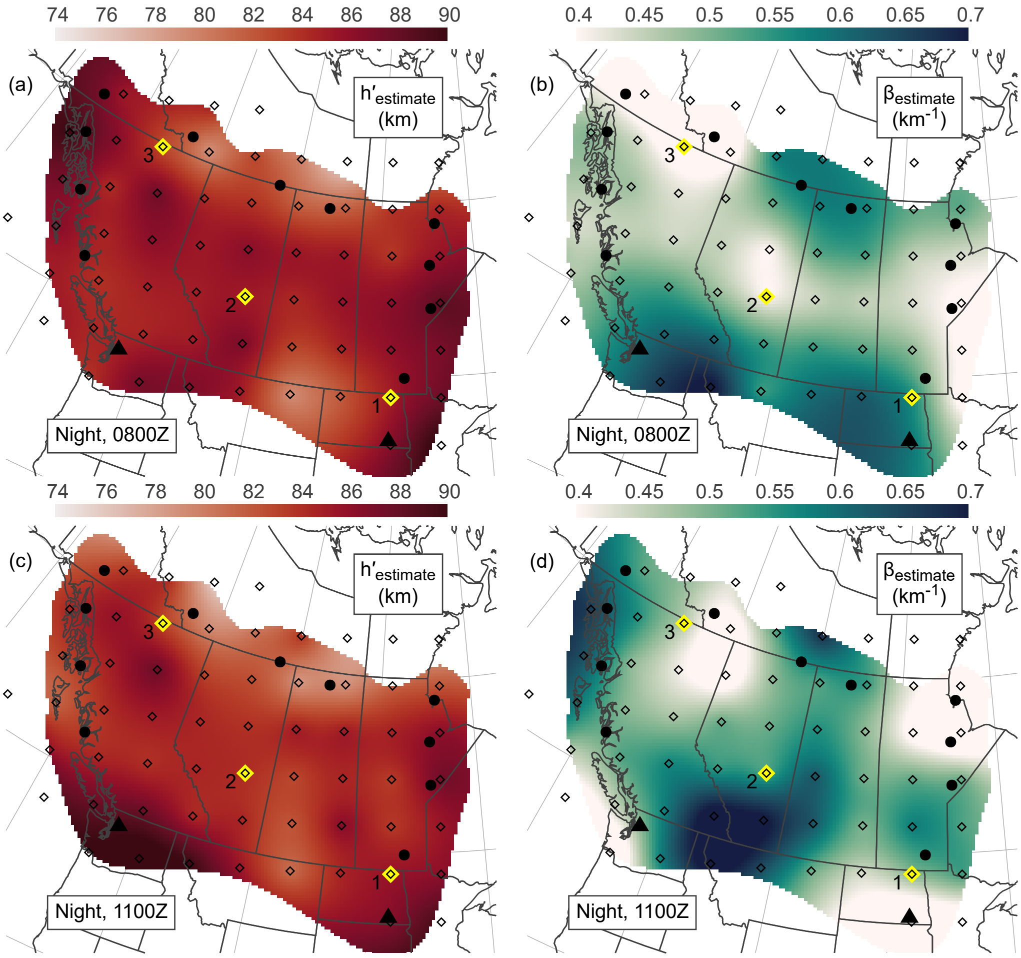

Figure A1. Estimated h' and β after six iterations of the LETKF. Subfigures (a) and (b) are for data simulated at 2020-03-02 0800Z and subfigures (c) and (d) are for data simulated at 2020-03-02 1100Z.

timates at these times continue to exhibit spatial variability (Fig. A1) and relatively high measurement residuals (Fig. A2). The true nighttime profiles have structure that is not captured by the exponential Wait profile estimated by the LETKF (Fig. A3).

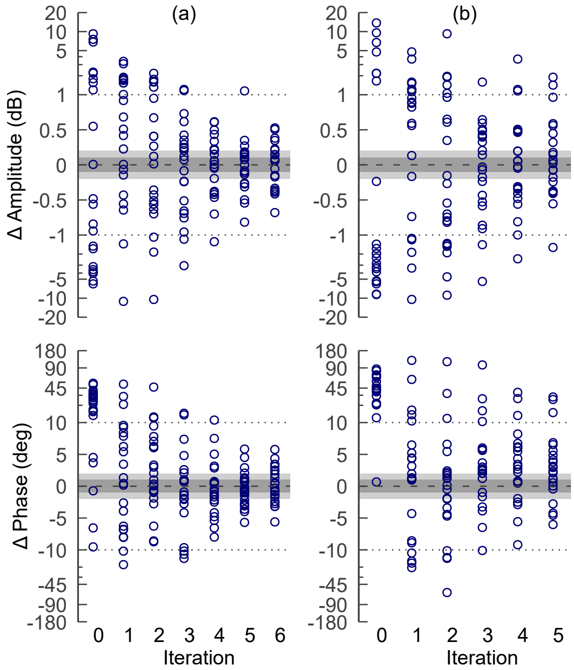

Figure A2. Amplitude (top) and phase (bottom) measurement residuals at each iteration of the LETKF for nighttime observations simulated at (a) 2020-03-02 0800Z and (b) 2020-03-02 1100Z.

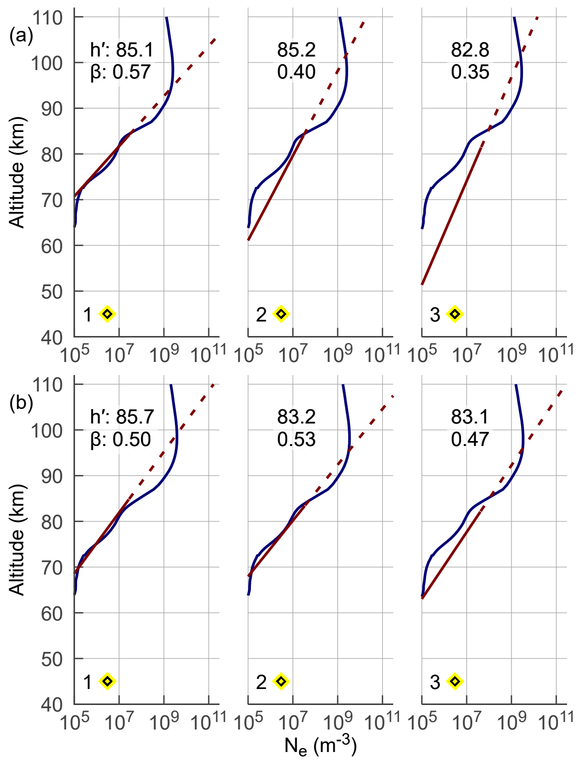

Figure A3. True and exponential estimated electron density profiles at the locations marked 1, 2, and 3 on Fig. A1 for observations simulated at (a) 2020-03-02 0800Z and (b) 2020-03-02 1100Z.

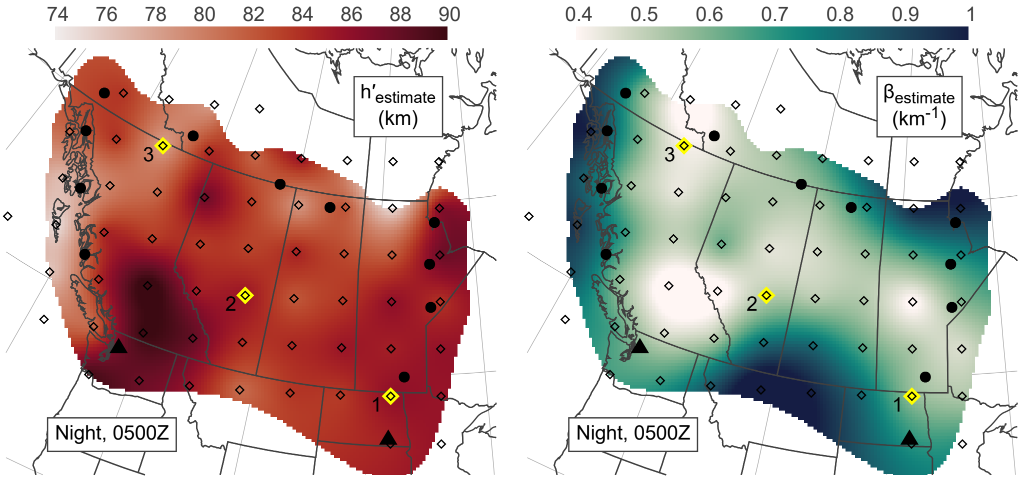

Figure B1. Estimated h' and β after six LETKF iterations of the nighttime ionosphere using a prior with constant $\beta = 0.9\,\mathrm{km}^{-1}$. Note the expanded color scale used in the β map compared to the other nighttime β maps.

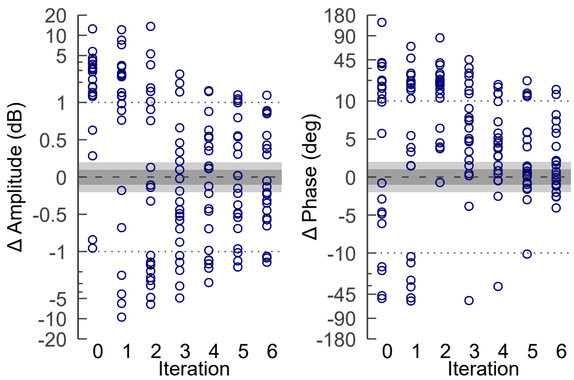

Figure B2. Measurement residuals at each iteration of the nighttime LETKF estimate using a prior with constant $\beta = 0.9\,\mathrm{km}^{-1}$.

Appendix B Alternative nighttime prior

Realistic nighttime ionosphere profiles are fit by an exponential profile with $\beta \approx 1\,\mathrm{km}^{-1}$ between electron densities of 10^7 and $10^9\,\mathrm{e}^-/\mathrm{m}^3$. In this section we present LETKF estimates for nighttime at 2020-03-02 0500Z that use a prior h' defined by the Ferguson model, Eq. (11), and a constant $\beta = 0.9\,\mathrm{km}^{-1}$. Figure B1 shows that the estimated h' has spatial structure that is not in the truth. The β estimate across the middle of the map decreases to approximately $0.5\,\mathrm{km}^{-1}$. The residuals, shown in Fig. B2, remain high.

Open Research

Data used to generate the figures in this article are available from Gasdia and Marshall (2022) at `https://zenodo.org/record/6549156`. Software to run the simulated observation experiments is available primarily in Gasdia (2022b) at `https://github.com/fgasdia/Imaging-EPP-with-VLF` and uses libraries in Gasdia (2022d, 2022a, 2022c, 2022e). For additional questions regarding the code, please contact the corresponding author at `Forrest.Gasdia@colorado.edu`.

Acknowledgments

This project was supported in part by a fellowship award through the National Defense Science and Engineering (NDSEG) Graduate Fellowship Program, sponsored by the Air Force Research Laboratory (AFRL), the Office of Naval Research (ONR), and the Army Research Office (ARO), and by NSF CAREER award AGS 2044846.

References

Anderson, B. R., Shekhar, S., Millan, R. M., Crew, A. B., Spence, H. E., Klumpar, D. M., … Turner, D. L. (2017, June). Spatial scale and duration of one microburst region on 13 August 2015. *Journal of Geophysical Research: Space Physics*, *122*(6), 5949–5964. doi: 10.1002/2016ja023752

Angelopoulos, V., Tsai, E., Bingley, L., Shaffer, C., Turner, D. L., Runov, A., … Zhang, G. Y. (2020, July). The ELFIN mission. *Space Science Reviews*, *216*(5), 103. doi: 10.1007/s11214-020-00721-7

Bilitza, D., Altadill, D., Truhlik, V., Shubin, V., Galkin, I., Reinisch, B., & Huang, X. (2017). International Reference Ionosphere 2016: From ionospheric climate to real-time weather predictions. *Space Weather*, *15*(2), 418–429. doi: 10.1002/2016sw001593

Blake, J. B., & O'Brien, T. P. (2016, April). Observations of small-scale latitudinal structure in energetic electron precipitation. *Journal of Geophysical Research: Space Physics*, *121*(4), 3031–3035. doi: 10.1002/2015ja021815

Blum, L. W., & Breneman, A. W. (2020). Observations of radiation belt losses due to cyclotron wave-particle interactions. In *The Dynamic Loss of Earth's Radiation Belts* (pp. 49–98). Elsevier. doi: 10.1016/b978-0-12-813371-2.00003-2

Buehner, M. (2020, June). Local ensemble transform Kalman filter with cross validation. *Monthly Weather Review*, *148*(6), 2265–2282. doi: 10.1175/mwr-d-19-0402.1

Chagas, R. A. J., de Sousa, F. L., Louro, A. C., & dos Santos, W. G. (2019, March). Modeling and design of a multidisciplinary simulator of the concept of operations for space mission pre-phase A studies. *Concurrent Engineering*, *27*(1), 28–39. doi: 10.1177/1063293X18804006

Chakraborty, S., Palit, S., Ray, S., & Chakrabarti, S. K. (2016, February). Modeling of the lower ionospheric response and VLF signal modulation during a total solar eclipse using ionospheric chemistry and LWPC. *Astrophysics and Space Science*, *361*(2), 72. doi: 10.1007/s10509-016-2660-0

Clilverd, M. A., Rodger, C. J., McCarthy, M., Millan, R., Blum, L. W., Cobbett, N., … Halford, A. J. (2017, January). Investigating energetic electron precipitation through combining ground-based and balloon observations. *Journal of Geophysical Research: Space Physics*, *122*(1), 534–546. doi: 10.1002/2016ja022812

Clilverd, M. A., Rodger, C. J., Thomson, N. R., Brundell, J. B., Ulich, T., Lichtenberger, J., … Turunen, E. (2009). Remote sensing space weather events: Antarctic-Arctic Radiation-belt (Dynamic) Deposition-VLF Atmospheric Research Konsortium network. *Space Weather*, *7*(4). doi: 10.1029/2008sw000412

Clilverd, M. A., Thomson, N. R., & Rodger, C. J. (1999). Sunrise effects on VLF signals propagating over a long north-south path. *Radio Science*, *34*(4), 939–948. doi: 10.1029/1999rs900052

Crew, A. B., Spence, H. E., Blake, J. B., Klumpar, D. M., Larsen, B. A., O'Brien, T. P., … Widholm, M. (2016, June). First multipoint in situ observations of electron microbursts: Initial results from the NSF FIREBIRD II mission. *Journal of Geophysical Research: Space Physics*, *121*(6), 5272–5283. doi: 10.1002/2016ja022485

Cully, C. M., Chaddock, D., Daniel, C., Davis, E., Galts, D., McGuffin, N., … Wilson, C. (2014, December). Early results on energetic particle precipitation observed by the ABOVE instrument array. *AGU Fall Meeting Abstracts*, *2014*, SA13B-3997.

Demirkol, M. K., Inan, U. S., Bell, T. F., Kanekal, S. G., & Wilkinson, D. C. (1999). Ionospheric effects of relativistic electron enhancement events. *Geophysical Research Letters*, *26*(23), 3557–3560. doi: 10.1029/1999GL010686

Ferguson, J. A. (1980, February). *Ionospheric profiles for predicting nighttime VLF/LF propagation* (techreport No. NOSC/TR-530). San Diego, CA: Naval Ocean Systems Center.

Ferguson, J. A. (1992, November). *A review of the ionospheric model for the Long Wave Prediction Capability* (techreport No. NCCOSC/RDT/E-TD-2393). San Diego, CA: Naval Command, Control, and Ocean Surveillance Center.

Ferguson, J. A. (1998, May). *Computer programs for assessment of long-wavelength radio communications, version 2.0: User's guide and source files* (techreport No. 3030). San Diego, CA: Space and Naval Warfare Systems Center.

Finlay, C. C., Kloss, C., Olsen, N., Hammer, M. D., Tøffner-Clausen, L., Grayver, A., & Kuvshinov, A. (2020, December). The CHAOS-7 geomagnetic field model and observed changes in the South Atlantic Anomaly. *Earth, Planets and Space*, *72*(1), 1–31. doi: 10.1186/s40623-020-01252-9

Friedrich, M., Pock, C., & Torkar, K. (2018, August). FIRI-2018, an updated empirical model of the lower ionosphere. *Journal of Geophysical Research: Space Physics*, *123*(8), 6737–6751. doi: 10.1029/2018ja025437

Friedrich, M., & Torkar, K. M. (2001). FIRI: A semiempirical model of the lower ionosphere. *Journal of Geophysical Research: Space Physics*, *106*(A10), 21409–21418. doi: 10.1029/2001ja900070

Gasdia, F. (2021). *Imaging the D-region ionosphere with subionospheric VLF signals* (phdthesis). University of Colorado Boulder.

Gasdia, F. (2022a). *EPPIonization.jl* [Software]. Zenodo. Retrieved from `https://github.com/fgasdia/EPPIonization.jl` doi: 10.5281/zenodo.6549109

Gasdia, F. (2022b). *FaradayInternationalReferenceIonosphere.jl* [Software]. Zenodo. Retrieved from `https://github.com/fgasdia/FaradayInternationalReferenceIonosphere.jl` doi: 10.5281/zenodo.6544857

Gasdia, F. (2022c). *Imaging-EPP-with-VLF.jl* [Software]. Zenodo. Retrieved from `https://github.com/fgasdia/Imaging-EPP-with-VLF` doi: 10.5281/zenodo.6549121

Gasdia, F. (2022d). *LongwaveModePropagator.jl* [Software]. Retrieved from `https://github.com/fgasdia/LongwaveModePropagator.jl`

Gasdia, F. (2022e). *SubionosphericVLFInversionAlgorithms.jl* [Software]. Zenodo. Retrieved from `https://github.com/fgasdia/SubionosphericVLFInversionAlgorithms.jl` doi: 10.5281/zenodo.6549127

Gasdia, F., & Marshall, R. A. (2019). Assimilating VLF transmitter observations with an LETKF for spatial estimates of the D-region ionosphere. *IEEE Transactions on Geoscience and Remote Sensing*, 1–18. doi: 10.1109/TGRS.2019.2957716

Gasdia, F., & Marshall, R. A. (2021, June). A new longwave mode propagator for the Earth-ionosphere waveguide. *IEEE Transactions on Antennas and Propagation*, 1–14. doi: 10.1109/tap.2021.3083753

Gasdia, F., & Marshall, R. A. (2022). *A method for imaging energetic particle precipitation with subionospheric VLF signals* [Dataset]. Zenodo. doi: 10.5281/ZENODO.6549156

Gaspari, G., & Cohn, S. E. (1999, January). Construction of correlation functions in two and three dimensions. *Quarterly Journal of the Royal Meteorological Society*, *125*(554), 723–757. doi: 10.1002/qj.49712555417

Ghaffari, R., Cully, C. M., Turner, D. L., & Reeves, G. D. (2020, November). Characteristics of electron precipitation during 40 energetic electron injections inferred via subionospheric VLF signal propagation. *Journal of Geophysical Research. Space Physics*, *125*(LA-UR-20-24385). doi: 10.1029/2019ja027233

Glukhov, V. S., Pasko, V. P., & Inan, U. S. (1992). Relaxation of transient lower ionospheric disturbances caused by lightning-whistler-induced electron precipitation bursts. *Journal of Geophysical Research: Space Physics*, *97*(A11), 16971–16979. doi: 10.1029/92ja01596

Houtekamer, P. L., & Zhang, F. (2016, June). Review of the ensemble Kalman filter for atmospheric data assimilation. *Monthly Weather Review*, *144*(12), 4489–4532. doi: 10.1175/mwr-d-15-0440.1

Hunt, B. R., Kostelich, E. J., & Szunyogh, I. (2007, June). Efficient data assimilation for spatiotemporal chaos: A local ensemble transform Kalman filter. *Physica D: Nonlinear Phenomena*, *230*(1), 112–126. doi: 10.1016/j.physd.2006.11.008

ITU-R. (2015, July). *World atlas of ground conductivities* (techreport No. P.832-4). Geneva: International Telecommunication Union. Retrieved from `https://www.itu.int/rec/R-REC-P.832/en`

Krause, L. H. (1998). *The interaction of relativistic electron beams with the near-Earth space environment* (phdthesis). University of Michigan.

Lehtinen, N. G., Bell, T. F., & Inan, U. S. (1999). Monte Carlo simulation of runaway MeV electron breakdown with application to red sprites and terrestrial gamma ray flashes. *Journal of Geophysical Research: Space Physics*, *104*(A11), 24699–24712. doi: 10.1029/1999ja900335

Lehtinen, N. G., & Inan, U. S. (2007). Possible persistent ionization caused by giant blue jets. *Geophysical Research Letters*, *34*(8). doi: 10.1029/2006gl029051

Ljungskog, E. (2021, July). *ScatteredInterpolation.jl.* Retrieved from `https://github.com/eljungsk/ScatteredInterpolation.jl`

Marshall, R. A., & Bortnik, J. (2018). Pitch angle dependence of energetic electron precipitation: energy deposition, backscatter, and the bounce loss cone. *Journal of Geophysical Research: Space Physics*, *123*(3), 2412–2423. doi: 10.1002/2017ja024873

Marshall, R. A., & Cully, C. M. (2020, January). Chapter 7 - Atmospheric effects and signatures of high-energy electron precipitation. In A. N. Jaynes & M. E. Usanova (Eds.), *The Dynamic Loss of Earth's Radiation Belts* (pp. 199–255). Elsevier. doi: 10.1016/B978-0-12-813371-2.00007-X

Marshall, R. A., Nicolls, M., Sanchez, E., Lehtinen, N. G., & Neilson, J. (2014). Diagnostics of an artificial relativistic electron beam interacting with the atmosphere. *Journal of Geophysical Research: Space Physics*, *119*(10), 8560–8577. doi: 10.1002/2014ja020427

Marshall, R. A., Wallace, T., & Turbe, M. (2017, December). Finite-difference modeling of very-low-frequency propagation in the earth-ionosphere waveguide. *IEEE Transactions on Antennas and Propagation*, *65*(12), 7185–7197. doi: 10.1109/tap.2017.2758392

Mauk, B. H., Fox, N. J., Kanekal, S. G., Kessel, R. L., Sibeck, D. G., & Ukhorskiy, A. (2013, November). Science objectives and rationale for the Radiation Belt Storm Probes mission. *Space Science Reviews*, *179*(1), 3–27. doi: 10.1007/s11214-012-9908-y

McCormick, J. C., & Cohen, M. B. (2018, March). D region ionospheric imaging using VLF/LF broadband sferics, forward modeling, and tomography. In *25th International Lightning Detection Conference & 7th International Lightning Meteorology Conference.*

McCormick, J. C., & Cohen, M. B. (2021, December). A new four-parameter D-region ionospheric model: Inferences from lightning-emitted VLF signals. *Journal of Geophysical Research: Space Physics*, *126*(12). doi: 10.1029/2021JA029849

McRae, W. M., & Thomson, N. R. (2000, May). VLF phase and amplitude: Daytime ionospheric parameters. *Journal of Atmospheric and Solar-Terrestrial Physics*, *62*(7), 609–618. doi: 10.1016/s1364-6826(00)00027-4

Millan, R. M., McCarthy, M. P., Sample, J. G., Smith, D. M., Thompson, L. D., McGaw, D. G., ... Hudson, M. K. (2013, November). The balloon array for RBSP relativistic electron losses (BARREL). *Space Science Reviews*, *179*(1), 503–530. doi: 10.1007/978-1-4899-7433-4_15

Millan, R. M., & Thorne, R. M. (2007, March). Review of radiation belt relativistic electron losses. *Journal of Atmospheric and Solar-Terrestrial Physics*, *69*(3), 362–377. doi: 10.1016/j.jastp.2006.06.019

Morgan, R. R. (1968, January). *World-wide VLF effective-conductivity map* (techreport No. WEST-80133F-1). Westinghouse Electric Corporation.

Pappert, R. A., & Smith, R. R. (1972). Orthogonality of VLF height gains in the Earth ionosphere waveguide. *Radio Science*, *7*(2), 275–278. doi: 10.1029/rs007i002p00275

Phanikumar, D. V., Maurya, A. K., Kumar, K. N., Venkatesham, K., Singh, R., Sharma, S., & Naja, M. (2018, June). Anomalous variations of VLF subionospheric signal and mesospheric ozone prior to 2015 Gorkha Nepal earthquake. *Scientific Reports*, *8*(1), 1–9. doi: 10.1038/s41598-018-27659-9

Picone, J. M., Hedin, A. E., Drob, D. P., & Aikin, A. C. (2002, December). NRLMSISE-00 empirical model of the atmosphere: Statistical comparisons and scientific issues. *Journal of Geophysical Research: Space Physics*, *107*(A12), 1–16. doi: 10.1029/2002ja009430

Randall, C. E., Harvey, V. L., Holt, L. A., Marsh, D. R., Kinnison, D., Funke, B., & Bernath, P. F. (2015). Simulation of energetic particle precipitation effects during the 2003–2004 Arctic winter. *Journal of Geophysical Research: Space Physics*, *120*(6), 5035–5048. doi: 10.1002/2015ja021196

Randall, C. E., Harvey, V. L., Manney, G. L., Orsolini, Y., Codrescu, M., Sioris, C., ... Russell, J. M. (2005). Stratospheric effects of energetic particle precipitation in 2003–2004. *Geophysical Research Letters*, *32*(5). doi: 10.1029/2004gl022003

Randall, C. E., Harvey, V. L., Singleton, C. S., Bailey, S. M., Bernath, P. F., Codrescu, M., ... Russell III, J. M. (2007). Energetic particle precipitation effects on the Southern Hemisphere stratosphere in 1992–2005. *Journal of Geophysical Research: Atmospheres*, *112*(D8). doi: 10.1029/2006jd007696

Ratcliffe, J. A. (1959). *The magneto-ionic theory & its applications to the ionosphere*. Cambridge: Cambridge University Press.

Rees, M. H. (1963, October). Auroral ionization and excitation by incident energetic electrons. *Planetary and Space Science*, *11*(10), 1209–1218. doi: 10/ctqn6t

Reeves, G. D., McAdams, K. L., Friedel, R. H. W., & O'Brien, T. P. (2003). Acceleration and loss of relativistic electrons during geomagnetic storms. *Geophysical Research Letters*, *30*(10). doi: 10.1029/2002gl016513

Rodger, C. J., Kavanagh, A. J., Clilverd, M. A., & Marple, S. R. (2013). Comparison between POES energetic electron precipitation observations and riometer absorptions: Implications for determining true precipitation fluxes. *Journal of Geophysical Research: Space Physics*, *118*(12), 7810–7821. doi: 10.1002/2013ja019439

Shumko, M., Sample, J., Johnson, A., Blake, B., Crew, A., Spence, H., ... Handley, M. (2018). Microburst scale size derived from multiple bounces of a microburst simultaneously observed with the FIREBIRD-II CubeSats. *Geophysical Research Letters*, *45*(17), 8811–8818. doi: 10.1029/2018gl078925

Silber, I., & Price, C. (2017, March). On the use of VLF narrowband measurements to study the lower ionosphere and the mesosphere–lower thermosphere. *Surveys in Geophysics*, *38*(2), 407–441. doi: 10.1007/s10712-016-9396-9

Thomson, N. R., Clilverd, M. A., & McRae, W. M. (2007). Nighttime ionospheric D region parameters from VLF phase and amplitude. *Journal of Geophysical Research: Space Physics*, *112*(A7), 1–14. doi: 10.1029/2007JA012271

Thomson, N. R., & McRae, W. M. (2009, August). Nighttime ionospheric D region: Equatorial and nonequatorial. *Journal of Geophysical Research: Space Physics*, *114*(A8), A08305. doi: 10.1029/2008JA014001

Thébault, E., Finlay, C. C., Beggan, C. D., Alken, P., Aubert, J., Barrois, O., … Zvereva, T. (2015, December). International Geomagnetic Reference Field: The 12th generation. *Earth, Planets and Space*, *67*(1), 1–19. doi: 10.1186/s40623-015-0228-9

Torkar, K. M., & Friedrich, M. (1983, June). Tests of an ion-chemical model of the D- and lower E-region. *Journal of Atmospheric and Terrestrial Physics*, *45*(6), 369–385. doi: 10.1016/s0021-9169(83)81097-6

Tu, W., Selesnick, R., Li, X., & Looper, M. (2010). Quantification of the precipitation loss of radiation belt electrons observed by SAMPEX. *Journal of Geophysical Research: Space Physics*, *115*(A7). doi: 10.1029/2009ja014949

Tyssøy, H. N., Sandanger, M. I., Ødegaard, L.-K. G., Stadsnes, J., Aasnes, A., & Zawedde, A. E. (2016). Energetic electron precipitation into the middle atmosphere—Constructing the loss cone fluxes from MEPED POES. *Journal of Geophysical Research: Space Physics*, *121*(6), 5693–5707. doi: 10.1002/2016ja022752

Wait, J. R. (1958, September). A study of VLF field strength data: Both old and new. *Geofisica pura e applicata*, *41*(1), 73–85. doi: 10.1007/bf01981861

Wait, J. R., & Spies, K. P. (1964, December). *Characteristics of the earth-ionosphere waveguide for VLF radio waves* (techreport No. 300). Boulder, CO: U.S. National Bureau of Standards. doi: 10.6028/nbs.tn.300

Whittaker, I. C., Gamble, R. J., Rodger, C. J., Clilverd, M. A., & Sauvaud, J.-A. (2013). Determining the spectra of radiation belt electron losses: Fitting DEMETER electron flux observations for typical and storm times. *Journal of Geophysical Research: Space Physics*, *118*(12), 7611–7623. doi: 10.1002/2013ja019228

Woodger, L. A., Halford, A. J., Millan, R. M., McCarthy, M. P., Smith, D. M., Bowers, G. S., … Liang, X. (2015). A summary of the BARREL campaigns: Technique for studying electron precipitation. *Journal of Geophysical Research: Space Physics*, *120*(6), 4922–4935. doi: 10.1002/2014ja020874

Xu, W., Marshall, R. A., Bortnik, J., & Bonnell, J. W. (2021). An electron density model of the D- and E-region ionosphere for transionospheric VLF propagation. *Journal of Geophysical Research: Space Physics*, *126*(7), e2021JA029288. doi: 10.1029/2021ja029288

Xu, W., Marshall, R. A., Fang, X., Turunen, E., & Kero, A. (2018). On the effects of bremsstrahlung radiation during energetic electron precipitation. *Geophysical Research Letters*, *45*(2), 1167–1176. doi: 10.1002/2017gl076510

Xu, W., Marshall, R. A., Kero, A., Turunen, E., Drob, D., Sojka, J., & Rice, D. (2019, October). VLF measurements and modeling of the D-region response to the 2017 total solar eclipse. *IEEE Transactions on Geoscience and Remote Sensing*, *57*(10), 7613–7622. doi: 10.1109/tgrs.2019.2914920

Xu, W., Marshall, R. A., Tyssøy, H. N., & Fang, X. (2020). A generalized method for calculating atmospheric ionization by energetic electron precipitation. *Journal of Geophysical Research: Space Physics*, *125*(11). doi: 10.1029/2020ja028482